High-Resolution Image Reconstruction With Displacement Errors: A Framelet Approach

Raymond H. Chan* Sherman D. Riemenschneider† Lixin Shen‡ Zuowei Shen§

Abstract

High-resolution image reconstruction arises in many applications, such as remote sensing, surveillance, and medical imaging. The model of Bose and Boo [2] can be viewed as the passage of the high-resolution image through a blurring kernel built from the tensor product of a univariate low-pass filter of the form $\left[\frac{1}{2}+\epsilon, 1, \cdots, 1, \frac{1}{2}-\epsilon\right]$, where ϵ is the displacement error. When the number L of low-resolution sensors is even, tight frame symmetric framelet filters were constructed in [9] from this low-pass filter using the unitary extension principle of [44]. The framelet filters do not depend on ϵ, and hence the resulting algorithm reduces to that of the case where $\epsilon = 0$. Furthermore, the framelet method works for symmetric boundary conditions. This greatly simplifies the algorithm. However, both the design of the tight framelets and extension to symmetric boundary are only for even L and cannot be applied to the case when L is odd. In this paper, we design tight framelets and derive a tight framelet algorithm with symmetric boundary conditions that work for both odd and even L. An analysis of the convergence of the algorithms is also given. The details of the implementations of the algorithm are also given.

1 Introduction

The resolution of digital images is a critical factor in many visual-communication related applications including remote sensing, military imaging, surveillance, medical imaging, and law enforcement. Although high-resolution (HR) images offer human observers accurate details of the target, the high cost of HR sensors is a factor as is the reliability of a single-node sensor. With an array of inexpensive low-resolution (LR) sensors positioned around the target, it becomes possible to use the information collected from distributed sources to reconstruct a desirable HR image at the destination. Much research has been done in the last three decades on the HR image reconstruction problems. Determined by the method of image reconstruction, previous work on high-resolution can be approximately classified into the following four major categories: frequency domain methods, interpolation-restoration methods, statistical based methods, and iterative spatial domain methods.

The earliest formulation of the problem was proposed by Huang and Tsay in [26] and was motivated by the need of improved resolution images from Landsat image data. They used the frequency

*Department of Mathematics, the Chinese University of Hong Kong, Shatin, NT, P. R. China. Email address: rchan@math.cuhk.edu.hk. Research supported in part by HKRGC Grant CUHK 400503 and CUHK DAG 2060257.

†Department of Mathematics, Armstrong Hall, P. O. Box 6310, West Virginia University, Morgantown, WV 26505. Email address: sherm@math.wvu.edu. This work was supported by grant NSF-EPSCoR-0132740. The work was partially done while this author was visiting the Institute for Mathematical Sciences, National University of Singapore in 2003. The visit was partially supported by the institute.

‡Department of Mathematics, Armstrong Hall, P. O. Box 6310, West Virginia University, Morgantown, WV 26505. Email address: lshen@math.wvu.edu. This work was supported under the grant NSF-EPSCoR-0132740.

§Department of Mathematics, National University of Singapore, 2 Science Drive 2, Singapore 117543. Research supported in part by several grants from the National University of Singapore.

domain approach to demonstrate reconstruction of one improved resolution image from several down-sampled noise-free versions of it. Kim *el al.* [30] suggested a simple generalization of this idea to noisy and blurred images using the aliasing relationship between the under-sampled LR frames and a reference frame to solve the problem by a weighted recursive least squares method. The frequency domain methods are intuitively simple and computationally cheap. However, they are extremely sensitive to model errors, and that limits their use [1]. This sensitivity to model errors has been improved by the development and use of a recursive total least squares (error-in-variables) algorithm in [3] to handle errors not only in observation but also errors in the estimation of shifts between frames.

Ur and Gross [50] applied Papoulis' [43] and Yen's [51] generalized multichannel sampling theorem to interpolate values on a higher resolution grid. Irain and Peleg [27, 28] employed iterative back projection method to iteratively update the HR estimate. Tekalp *et al.* [48, 49] and Stark and Oskoui [47] used the theory of Projection-Onto-Convex-Sets to solve the problem of restoration and interpolation. Nguyen *et al.* [40] developed a super-resolution algorithm by interpolating interlaced data using wavelets. Recently, Lertrattanapanich and Bose [32] proposed a so-called Delaunay triangulation interpolation method for high-resolution image reconstruction.

Statistical models for super-resolution image reconstruction problems have appeared in the literature recently. Schultz and Stevenson [45] used Maximum a Posteriori (MAP) estimator with the Huber-Markov Random Filed prior. Hardie *et al.* [24] proposed a joint MAP registration and restoration algorithm using a Gibbs image prior.

Iterative spatial domain methods are popular class of methods for solving the problems of resolution enhancement [2, 20, 21, 22, 25, 31, 35, 38, 39, 42]. The problems are formulated as Tikhonov regularization. Much work has been devoted to the efficient calculation of the reconstruction and the estimation of the associated hyperparameters by taking advantage of the inherent structures in the HR system matrix. Bose and Boo [2] use a block semi-circulant matrix decomposition in order to calculate the MAP reconstruction. Ng *et al.* [35] and Ng and Yip [37] proposed a fast DCT-based approach for HR image reconstruction with Neumann boundary condition. Nguyen *et al.* [41, 42] also addressed the problem of efficient calculation. The proper choice of the regularization tuning parameter is crucial to achieving robustness in the presence of noise and avoiding trial-and-error in the selection of an optimal tuning parameter. To this end, Bose *et al.* [4] used a L-curve based approach. Nguyen *et al.* [42] used a generalized cross-validation method. Molona *et al.* [33] used an EM algorithm.

The reconstruction of HR images from multiple LR image frames can be modeled by

$$g = Hf + \eta \tag{1}$$

where f is the desired HR image, H is the blurring kernel, g is the observed HR image formed from the low-resolution images, and η is noise. Recently, new approaches for HR image reconstruction problems using wavelet techniques have been proposed by Chan *et al.* in [6, 7, 8]. The problem of HR image reconstruction is understood and analyzed under the framework of multi-resolution analysis of $\mathcal{L}^2(\mathbb{R}^2)$ by recognizing the blurring kernel H as a low-pass filter associated with a multi-resolution analysis. This low-pass filter is a tensor product of the univariate low-pass filter:

$$_{L,\epsilon}m_0 = \frac{1}{L}\left[\frac{1}{2}+\epsilon, \overbrace{1,\cdots,1}^{L-1}, \frac{1}{2}-\epsilon\right] \tag{2}$$

where the parameter ϵ is different in the x and y directions for each sensor.

The reasoning within the wavelet framework provides the intuition for new algorithms. The wavelet-based HR image reconstruction algorithms in [6, 7, 8] are developed through the perfect reconstruction formula of a bi-orthogonal wavelet system which has (2) as its primary low-pass filter. The algorithms approximate iteratively the wavelet coefficients folded by the given low-pass filter. By incorporating the wavelet analysis viewpoint, many available techniques developed in the wavelet literature, such as wavelet-based denoising schemes, can be applied to the problem. The first requirement is the construction of a bi-orthogonal wavelet system with (2) as its primary low-pass filter. Examples for $L = 2$ and 4 are given in [7] for $\epsilon = 0$ and in [8] for $\epsilon \neq 0$. Minimally supported bi-orthogonal wavelet systems with (2) as primary low-pass filter are constructed for arbitrary integer $L \geq 2$ and any real number $|\epsilon| < 1/2$ in [46]. For the case without displacement error (i.e., when all $\epsilon = 0$), the corresponding blurring kernel H is spatially invariant and (1) is actually a de-convolution problem. The proposed algorithm in [7] outperforms the least squares method in terms of peak signal-to-noise ratio (PSNR).

For the case with displacement error (i.e., some $\epsilon \neq 0$), the corresponding blurring kernel H is spatially variant. The performance of the proposed algorithm in [8] is comparable with that of the least squares method. We note that the algorithm in [8] is a nontrivial extension of the algorithmic framework of [7], which applies only to spatially invariant blurring operators. There are several issues affecting the performance of the wavelet approach for problems with displacement errors. First, the design of the filters ${}_{L,\epsilon}m_0$ is related to displacement errors. As shown in [7, 8], the image is represented in the multiresolution analysis generated by a dual low-pass filter, the regularity of the dual scaling function plays a key role in the performance of wavelet-based algorithms. However, the regularity of scaling functions varies with the displacement errors, and in some cases, the function can even be discontinuous [46]. Although the regularity can be improved by increasing the vanishing moments of the dual low-pass filter, it would produce ringing effects and increase the computational complexity. Second, since the filters ${}_{L,\epsilon}m_0$ are not symmetric, we can only impose periodic boundary conditions. However, numerical results from both the least squares and wavelet methods show that symmetric boundary conditions usually provide much better performance than do periodic boundary conditions (e.g., [7, 8, 36]).

To overcome these two problems, we proposed a new algorithm based on a tight framelet system for every even number L (see [9]). The key idea is to decompose the low-pass filter ${}_{L,\epsilon}m_0$ into a low-pass filter (corresponding to $\epsilon = 0$) and a high-pass filter. More precisely,

$$ {}_{L,\epsilon}m_0 = {}_L\tau_0 + \sqrt{2}\epsilon\, {}_L\tau_1, \tag{3} $$

where

$$ {}_L\tau_0 = \frac{1}{2L}[1, \overbrace{2, \cdots, 2}^{L-1}, 1] \quad \text{and} \quad {}_L\tau_1 = \frac{\sqrt{2}}{2L}[1, \overbrace{0, \cdots, 0}^{L-1}, -1]. \tag{4} $$

The construction of the tight framelet system with ${}_L\tau_0$ as low-pass filter and ${}_L\tau_1$ as one of its high-pass filters can be given explicitly for even integers $L \geq 2$ through piecewise linear tight framelets (see [9]). Numerical experiments there show that the framelet approach is much better than the wavelet approach in [7, 8]. This current paper was necessitated because both the design of tight framelets with (2) as its low-pass filter and the extension to symmetric boundary conditions in [9] could not be applied to the case when L is odd.

The outline of the paper is as follows. In §2, we introduce the model by Bose and Boo [2]. In §3, we construct tight framelet systems for HR image reconstruction. An analysis of the convergence of the algorithms is also given. Matrix implementations of the designed tight framelet are given under symmetric boundary conditions in §4. Tight framelet based HR image reconstruction algorithms are developed in §5. Numerical experiments are illustrated in §6. Finally, our conclusion is given in §7.

For the rest of the paper, we will use the following notations. Bold-faced characters indicate vectors and matrices. The numbering of matrix and vector starts from 0. The matrix $\mathbf{L}^t$ denotes the transpose of the matrix $\mathbf{L}$. The symbols $\mathbf{I}$ and $\mathbf{0}$ denote the identity and zero matrices respectively. For a given function $f \in \mathcal{L}^1(\mathbb{R})$, $\widehat{f}(\omega) = \int_{\mathbb{R}} f(x)e^{-jx\omega}dx$ denotes the Fourier transform of f. For a given sequence m, $\widehat{m}(\omega) = \sum_{k\in\mathbb{Z}} m(k)e^{-jk\omega}$ denotes the Fourier series of m, and $\overline{\widehat{m}}$ denotes the complex conjugate of $\widehat{m}$. The Kronecker delta function is $\delta_{k,l} = 1$ if $k = l$ and 0 otherwise.

To describe Toeplitz and Hankel matrices, we use the following notations:

$$\text{Toeplitz}(\mathbf{a}, \mathbf{b}) = \begin{pmatrix} a_0 & a_1 & \cdots & a_{N-2} & a_{N-1} \\ b_1 & a_0 & \cdots & a_{N-3} & a_{N-2} \\ \vdots & \vdots & \ddots & \vdots & \vdots \\ b_{N-2} & b_{N-3} & \cdots & a_0 & a_1 \\ b_{N-1} & b_{N-2} & \cdots & b_1 & a_0 \end{pmatrix}, \quad \text{with} \quad a_0 = b_0,$$

and

$$\text{Hankel}(\mathbf{a}, \mathbf{b}) = \begin{pmatrix} a_0 & a_1 & \cdots & a_{N-2} & a_{N-1} \\ a_1 & a_2 & \cdots & a_{N-1} & b_{N-2} \\ \vdots & \vdots & \ddots & \vdots & \vdots \\ a_{N-2} & a_{N-1} & \cdots & b_2 & b_1 \\ a_{N-1} & b_{N-2} & \cdots & b_1 & b_0 \end{pmatrix}, \quad \text{with} \quad a_{N-1} = b_{N-1}.$$

The matrix PseudoHankel$(\mathbf{a}, \mathbf{b})$ is formed from Hankel$(\mathbf{a}, \mathbf{b})$ by replacing both the first column and the last column with zero vectors, i.e.,

$$\text{PseudoHankel}(\mathbf{a}, \mathbf{b}) = \begin{pmatrix} 0 & a_1 & \cdots & a_{N-2} & 0 \\ 0 & a_2 & \cdots & a_{N-1} & 0 \\ \vdots & \vdots & \ddots & \vdots & \vdots \\ 0 & a_{N-1} & \cdots & b_2 & 0 \\ 0 & b_{N-2} & \cdots & b_1 & 0 \end{pmatrix}, \quad \text{with} \quad a_{N-1} = b_{N-1}.$$

2 Mathematical Model for High-Resolution Image Reconstruction

The system (1) is ill-posed. Usually it is solved by Tikhonov's regularization method. The Tikhonov-regularized solution is defined to be the unique minimizer of

$$\min_f \left\{ \|Hf - g\|^2 + \alpha R(f) \right\} \tag{5}$$

where $R(f)$ is a regularization functional. The basic idea of regularization is to replace the original ill-posed problem with a "nearby" well-posed problem whose solution approximates the required solution. The regularization parameter α provides a tradeoff between fidelity to the measurements and noise sensitivity. High-resolution reconstruction consists of two separate problems: image registration and image reconstruction. Image registration refers to the estimation of relative displacements with respect to the reference low-resolution frame; and image reconstruction refers to the stage of restoring the HR image. In this paper, we focus on the case where the registration is not required.

We follow the high-resolution reconstruction model proposed by Bose and Boo [2]. Consider a sensor array with $L \times L$ sensors in which each sensor has $N_1 \times N_2$ sensing elements and the size of each sensing element is $T_1 \times T_2$. Our aim is to reconstruct an image with resolution $M_1 \times M_2$, where $M_1 = L \times N_1$ and $M_2 = L \times N_2$.

In order to have enough information to resolve the high-resolution image, there are subpixel displacements between the sensors in the sensor arrays. For sensor (ℓ_1, ℓ_2), $0 \le \ell_1, \ell_2 < L$ with $(\ell_1, \ell_2) \ne (0,0)$, its vertical and horizontal displacements $d^x_{\ell_1,\ell_2}$ and $d^y_{\ell_1,\ell_2}$ with respect to the $(0,0)$th reference sensor are given by

$$d^x_{\ell_1,\ell_2} = \left(\ell_1 + \epsilon^x_{\ell_1,\ell_2}\right)\frac{T_1}{L} \quad \text{and} \quad d^y_{\ell_1,\ell_2} = \left(\ell_2 + \epsilon^y_{\ell_1,\ell_2}\right)\frac{T_2}{L}.$$

Here $\epsilon^x_{\ell_1,\ell_2}$ and $\epsilon^y_{\ell_1,\ell_2}$ are the vertical and horizontal *displacement errors* respectively. We assume that

$$|\epsilon^x_{\ell_1,\ell_2}| < \frac{1}{2} \quad \text{and} \quad |\epsilon^y_{\ell_1,\ell_2}| < \frac{1}{2}.$$

For sensor (ℓ_1, ℓ_2), the average intensity registered at its (n_1, n_2)th pixel is modeled by:

$$g_{\ell_1,\ell_2}[n_1,n_2] = \frac{1}{T_1 T_2}\int_{T_1(n_1-1/2)+d^x_{\ell_1,\ell_2}}^{T_1(n_1+1/2)+d^x_{\ell_1,\ell_2}} \int_{T_2(n_2-1/2)+d^y_{\ell_1,\ell_2}}^{T_2(n_2+1/2)+d^y_{\ell_1,\ell_2}} f(x,y)dxdy + \eta_{\ell_1,\ell_2}[n_1,n_2]. \tag{6}$$

Here $0 \le n_1 < N_1$ and $0 \le n_2 < N_2$ and $\eta_{\ell_1,\ell_2}[n_1,n_2]$ is the noise, see [2]. We intersperse all the low-resolution images g_{ℓ_1,ℓ_2} to form an $M_1 \times M_2$ image g by assigning

$$g[Ln_1 + \ell_1, Ln_2 + \ell_2] = g_{\ell_1,\ell_2}[n_1,n_2].$$

The image g is already a high-resolution image and is called the *observed high-resolution image*. It is already a better image than any one of the low-resolution samples g_{ℓ_1,ℓ_2} themselves, c.f. the figures in the second row with those in the first row in Figures 4–7.

To obtain an even better image than g (e.g. figures in the bottom two rows in Figures 4–7), one will have to find f from (6). One way is to discretize (6) using the rectangular quadrature rule and then solve the discrete system for f. Since the right hand side of (6) involves the values of f outside the scene (i.e. outside the domain of g), the resulting system will have more unknowns than the number of equations, and one has to impose boundary conditions on f for points outside the scene, see e.g. [2]. Then the blurring matrix corresponding to the (ℓ_1, ℓ_2)th sensor is given by a square matrix of the form

$$\mathbf{H}_{\ell_1,\ell_2}(\epsilon^x_{\ell_1,\ell_2}, \epsilon^y_{\ell_1,\ell_2}) = \mathbf{H}^y(\epsilon^y_{\ell_1,\ell_2}) \otimes \mathbf{H}^x(\epsilon^x_{\ell_1,\ell_2}). \tag{7}$$

The matrices $\mathbf{H}^x(\epsilon^x_{\ell_1,\ell_2})$ and $\mathbf{H}^y(\epsilon^y_{\ell_1,\ell_2})$ vary under different boundary conditions and will be given later.

The blurring matrix for the whole sensor array is made up of blurring matrices from each sensor:

$$\mathbf{H}(\boldsymbol{\epsilon}^x, \boldsymbol{\epsilon}^y) = \sum_{\ell_1=0}^{L-1}\sum_{\ell_2=0}^{L-1} \mathbf{D}_{\ell_1,\ell_2}\mathbf{H}_{\ell_1,\ell_2}(\epsilon^x_{\ell_1,\ell_2}, \epsilon^y_{\ell_1,\ell_2}) \tag{8}$$

where $\boldsymbol{\epsilon}^x = [\epsilon^x_{\ell_1,\ell_2}]_{\ell_1,\ell_2=0}^{L-1}$ and $\boldsymbol{\epsilon}^y = [\epsilon^y_{\ell_1,\ell_2}]_{\ell_1,\ell_2=0}^{L-1}$. Here $\mathbf{D}_{\ell_1,\ell_2}$ is the sampling matrix for the (ℓ_1, ℓ_2)th sensor, and is given by

$$\mathbf{D}_{\ell_1,\ell_2} = \mathbf{D}_{\ell_2} \otimes \mathbf{D}_{\ell_1} \tag{9}$$

where $\mathbf{D}_{\ell_j} = \mathbf{I}_{N_j} \otimes \mathbf{e}^t_{\ell_j}$ with $\mathbf{e}_{\ell_j}$ the j-th unit vector.

Let $\mathbf{f}$ and $\mathbf{g}$ be the column vectors formed by f and g. The model of the reconstruction of high-resolution images from multiple low-resolution image frames becomes

$$\mathbf{g} = \mathbf{H}(\boldsymbol{\epsilon}^x, \boldsymbol{\epsilon}^y)\mathbf{f} + \eta. \tag{10}$$

The Tikhonov-regularization model in (5) becomes

$$(\mathbf{H}(\boldsymbol{\epsilon}^x, \boldsymbol{\epsilon}^y)^t \mathbf{H}(\boldsymbol{\epsilon}^x, \boldsymbol{\epsilon}^y) + \alpha \mathbf{R})\mathbf{f} = \mathbf{H}(\boldsymbol{\epsilon}^x, \boldsymbol{\epsilon}^y)^t \mathbf{g} \tag{11}$$

where $\mathbf{R}$ is the matrix corresponding to the regularization functional R in (5).

Several different methods have been proposed to solve the system (10) in the literature. In the case of no displacement errors, i.e. $\boldsymbol{\epsilon}^x = \boldsymbol{\epsilon}^y = \mathbf{0}$, the blurring matrix $\mathbf{H}(\mathbf{0}, \mathbf{0})$ in (10) exhibits very rich algebraic structure. In fact, by imposing traditional zero-padding boundary condition, $\mathbf{H}(\mathbf{0}, \mathbf{0})$ is a block-Toeplitz-Toeplitz-block matrix (see [2]). By imposing the periodic boundary condition, $\mathbf{H}(\mathbf{0}, \mathbf{0})$ in (10) is a block-circulant-circulant-block matrix. The resulting Tikhonov system (11) is then solved by fast Fourier transform. By imposing Neumann boundary condition, $\mathbf{H}(\mathbf{0}, \mathbf{0})$ in (10) is a block Toeplitz-plus-Hankel with Toeplitz-plus-Hankel blocks. The resulting Tikhonov system (11) is then solved by fast cosine transform in [35]. In the case with displacement errors, one can use the matrices $\mathbf{H}(\mathbf{0}, \mathbf{0})$ as a preconditioner for $\mathbf{H}(\boldsymbol{\epsilon}^x, \boldsymbol{\epsilon}^y)$, and solve the systems by the preconditioned conjugate gradient method, see [2, 34].

A different viewpoint was proposed in [7, 8] for understanding (10). By (8), the observed image $\mathbf{g}$ is formed by sampling and summing different blurring images $\mathbf{H}_{\ell_1,\ell_2}(\epsilon^x_{\ell_1,\ell_2}, \epsilon^y_{\ell_1,\ell_2})\mathbf{f}$. The low-resolution image $\mathbf{D}_{\ell_1,\ell_2}\mathbf{H}_{\ell_1,\ell_2}(\epsilon^x_{\ell_1,\ell_2}, \epsilon^y_{\ell_1,\ell_2})\mathbf{f}$, which results from the sampling of $\mathbf{H}_{\ell_1,\ell_2}(\epsilon^x_{\ell_1,\ell_2}, \epsilon^y_{\ell_1,\ell_2})\mathbf{f}$, is considered as the output of the image $\mathbf{f}$ passing through a low-pass filter which associates with a multiresolution analysis of $\mathcal{L}^2(\mathbb{R}^2)$. An algorithm was then derived to solve the problem (10) using low-pass filters and their duals [7, 8].

3 Tight Framelet Systems and Analysis of Algorithms

No matter which boundary condition is imposed on the model, the interior row of $\mathbf{H}^x(\epsilon^x_{\ell_1,\ell_2})$ (similarly of $\mathbf{H}^y(\epsilon^y_{\ell_1,\ell_2})$) is given by

$$\frac{1}{L}\left[0, \cdots, 0, \frac{1}{2} + \epsilon^x_{\ell_1,\ell_2}, \overbrace{1, \cdots, 1}^{L-1}, \frac{1}{2} - \epsilon^x_{\ell_1,\ell_2}, 0, \cdots, 0\right]. \tag{12}$$

This motivated us in [7, 8] to consider the blurring matrix $\mathbf{H}^y(\epsilon^y_{\ell_1,\ell_2}) \otimes \mathbf{H}^x(\epsilon^x_{\ell_1,\ell_2})$ as a low-pass filter acting on the image f. This low-pass filter is a tensor product of the univariate low-pass filter (2). Using this observation, wavelet algorithms based on bi-orthogonal wavelet systems were proposed in [7, 8] and a tight framelet based algorithm was then developed in [9]. The numerical experiments in [9] illustrated the effectiveness of the tight framelet based HR image reconstruction over the wavelet approach in [7, 8]. However, in [9], we only consider the case where L is even. In fact, both the approach for designing tight framelets with (12) as its low-pass filter and the symmetric boundary extension for even number L given in [9] cannot be applied to the case of odd number L. In this section, we will give a different method from [9] to derive the tight framelets for an arbitrary integer L. Two algorithms are also proposed in the Fourier domain.

3.1 Tight framelet system

The construction of compactly supported (bi-)orthonormal wavelet bases of arbitrarily high smoothness has been widely studied since Ingrid Daubechies's celebrated works [13, 14]. Tight frames generalize orthonormal systems and give more flexibility in filter designs. A system $X \subset \mathcal{L}^2(\mathbb{R})$ is called a tight frame of $\mathcal{L}^2(\mathbb{R})$ if

$$\sum_{h \in X} |\langle f, h\rangle|^2 = \|f\|^2,$$

holds for all $f \in \mathcal{L}^2(\mathbb{R})$, where $\langle \cdot, \cdot \rangle$ and $\|\cdot\| = \langle \cdot, \cdot \rangle^{1/2}$ are the inner product and norm of $\mathcal{L}^2(\mathbb{R})$. This is equivalent to

$$\sum_{h \in X} \langle f, h\rangle h = f, \quad f \in \mathcal{L}^2(\mathbb{R}).$$

Hence, like an orthonormal system, one can use the same system X for both the decomposition and reconstruction processes. They preserve the unitary property of the relevant analysis and synthesis operators, while sacrificing the orthonormality and the linear independence of the system in order to get more flexibility.

If X is the collection of dilations of L^j, $j \in \mathbb{Z}$, and shifts of a finite set $\Psi \subset \mathcal{L}^2(\mathbb{R})$, i.e.,

$$X(\Psi) = \{\psi^\ell_{j,k} : \psi \in \Psi, 1 \le \ell \le r; j, k \in \mathbb{Z}\}, \tag{13}$$

where $\psi^\ell_{j,k}(t) = L^{j/2}\psi^\ell(L^j \cdot -k)$, then $X(\Psi)$ is called, in general, a wavelet system. When $X(\Psi)$ forms an orthonormal basis of $\mathcal{L}^2(\mathbb{R})$, it is called an orthonormal wavelet system. In this case the elements in Ψ are called the orthonormal wavelets. When $X(\Psi)$ is a tight frame for $\mathcal{L}^2(\mathbb{R})$ and Ψ is generated via a multiresoultaion analysis, then each element of Ψ is called a tight framelet, and $X(\Psi)$ is called a tight framelet system. Tight framelet systems generalize orthonormal wavelet systems.

3.2 Construction of tight framelets

The low-pass filter in (12), denoted by ${}_{L,\epsilon}m_0$, can be considered as a combination of a low-pass filter (corresponding to $\epsilon = 0$) and a high-pass filter. More precisely,

$${}_{L,\epsilon}m_0 \equiv \frac{1}{L}\left[\frac{1}{2}+\epsilon, \overbrace{1, \cdots, 1}^{L-1}, \frac{1}{2}-\epsilon\right] = {}_Lm_0 + 2\epsilon\, {}_Lm_1, \tag{14}$$

where

$${}_Lm_0 = \frac{1}{2L}[1, \overbrace{2, \cdots, 2}^{L-1}, 1] \quad \text{and} \quad {}_Lm_1 = \frac{1}{2L}[1, \overbrace{0, \cdots, 0}^{L-1}, -1]. \tag{15}$$

Note that ${}_Lm_0$ in (15) is the same as ${}_L\tau_0$ in (4). However, ${}_Lm_1$ in (15) differs from ${}_L\tau_1$ in (4) by a factor of $\sqrt{2}$.

Let

$${}_L\widehat{\phi}(\omega) = \prod_{k=1}^{+\infty} {}_Lm_0(\omega/L^k).$$

Then ${}_L\phi$ is a compactly supported scaling function with dilation L, and ${}_Lm_0$ is the low-pass filter associated with the scaling function ${}_L\phi$. Moreover, ${}_L\phi$ is Hölder continuous with Hölder exponent of $\ln 2/\ln L$, see [46]. Furthermore, the sequence of spaces defined by

$$V_0 = \overline{\operatorname{span}\{\phi(\cdot - k) : k \in \mathbb{Z}\}}, \quad V_j = \{h(L^j \cdot) : h \in V_0\}, \quad j \in \mathbb{Z}$$

forms a multiresolution analysis. Recall that a multiresolution analysis (MRA) generated by ϕ is a family of closed subspaces $\{V_j\}_{j\in\mathbb{Z}}$ of $\mathcal{L}^2(\mathbb{R})$ that satisfies: (i) $V_j \subset V_{j+1}$, (ii) $\bigcup_j V_j$ is dense in $\mathcal{L}^2(\mathbb{R})$, and (iii) $\bigcap_j V_j = \{0\}$ (see [17] and [29]).

Our purpose is then to construct a tight framelet system with ${}_Lm_0$ as a low-pass filter and ${}_Lm_1$ high-pass filter. There is a growing interest in construction tight framelets derived from refinable functions since Ron and Shen suggested the 'Unitary Extension Principle' in [44]. Recently, the unitary extension principle was further extended independently by Daubechies, Han, Ron and Shen in [16] and Chui, He and Stöckler in [12] to the Oblique Extension Principle. These two principles lead to some systematic constructions of tight framelets from MRA generated by various refinable functions (see [11, 12, 16, 23, 44]). Here, we will use the unitary extension principle to design a tight framelet system from a given refinable function and a wavelet generator. The motivation for considering this problem is derived from our practical requirement as mentioned above.

To present our result, let us introduce some further notations. We start with the low-pass filter corresponding to the Haar wavelet with dilation P,

$$ {}_P\mathrm{Haar}_0 = \frac{1}{P}[1, 1, \cdots, 1]. $$

Then, the corresponding (orthonormal) Haar wavelet masks (high-pass filters) can be obtained via DCT III as

$$ {}_P\mathrm{Haar}_p = \frac{\sqrt{2}}{P}\left[\cos\left(\frac{p\pi}{2P}\right), \cos\left(\frac{3p\pi}{2P}\right), \cdots, \cos\left(\frac{(2P-1)p\pi}{2P}\right)\right], \quad p = 1, \ldots P-1. $$

Further, they satisfy

$$ \sum_{p=0}^{P-1} {}_P\widehat{\mathrm{Haar}}_p(\omega)\, \overline{{}_P\widehat{\mathrm{Haar}}_p(\omega + \frac{2\pi\ell}{P})} = \delta_{\ell,0}, \quad \ell = 0, \ldots, P-1, \tag{16} $$

where ${}_P\widehat{\mathrm{Haar}}_p$ is the Fourier series of ${}_P\mathrm{Haar}_p$, $p = 0, 1 \ldots, P-1$.

Now we can design a tight framelets with ${}_Lm_0$ as low-pass filter and ${}_Lm_1$ as one of its high-pass filters. The basic idea is that the filter ${}_Lm_0$ and ${}_Lm_1$ can be interpreted as the sum and difference of the elementary filter $\frac{1}{L}[1, \ldots, 1]$. For example, for $L = 4$, we have

$$ \begin{aligned} \frac{1}{2L}[1, 2, 2, 2, 1] &= \frac{1}{2L}[1, 1, 1, 1, 0] + \frac{1}{2L}[0, 1, 1, 1, 1], \\ \frac{1}{2L}[1, 0, 0, 0, -1] &= \frac{1}{2L}[1, 1, 1, 1, 0] - \frac{1}{2L}[0, 1, 1, 1, 1]. \end{aligned} $$

That is, in the Fourier domain

$$ {}_4\widehat{m}_0(\omega) = {}_2\widehat{\mathrm{Haar}}_0(\omega)\, {}_4\widehat{\mathrm{Haar}}_0(\omega), \quad \text{and} \quad {}_4\widehat{m}_1(\omega) = {}_2\widehat{\mathrm{Haar}}_1(\omega)\, {}_4\widehat{\mathrm{Haar}}_0(\omega). $$

In general, for an arbitrary L, we have

$$ {}_L\widehat{m}_0(\omega) = {}_2\widehat{\mathrm{Haar}}_0(\omega)\, {}_L\widehat{\mathrm{Haar}}_0(\omega), \quad \text{and} \quad {}_L\widehat{m}_1(\omega) = {}_2\widehat{\mathrm{Haar}}_1(\omega)\, {}_L\widehat{\mathrm{Haar}}_0(\omega). $$

Motivated from the above equations, we define

$$ {}_L\widehat{m}_{2p+q}(\omega) = {}_2\widehat{\mathrm{Haar}}_q(\omega)\, {}_L\widehat{\mathrm{Haar}}_p(\omega) \tag{17} $$

where $q \in \{0,1\}$ and $p = 0, \ldots, L-1$. It follows from (16) that

$$\sum_{q=0}^{1} \sum_{p=0}^{L-1} {}_L\widehat{m}_{2p+q}(\omega)\, \overline{{}_L\widehat{m}_{2p+q}\left(\omega + \frac{2\pi\ell}{L}\right)} = \delta_{\ell,0}, \quad \ell = 0, \ldots, L-1. \tag{18}$$

With this, the Unitary Extension Principle of [44] implies that the functions

$$\Psi = \{\, {}_L\psi_{2p+q} : 0 \le p \le L-1, \quad q = 0, 1, \quad (p,q) \neq (0,0)\}$$

defined by

$${}_L\widehat{\psi}_{2p+q}(\omega) = {}_L\widehat{m}_{2p+q}\left(\frac{\omega}{2}\right) {}_L\widehat{\phi}\left(\frac{\omega}{2}\right).$$

are tight framelets. That is

$$X(\Psi) = \left\{ L^{k/2}\psi_{2p+q}(L^k \cdot -j) : 0 \le p \le L-1, q = 0, 1, (p,q) \neq (0,0); k, j \in \mathbb{Z} \right\}$$

is a tight frame system of $\mathcal{L}^2(\mathbb{R})$. The framelet ${}_L\psi_{2p+q}$ is either symmetric or anti-symmetric. Hence, the symmetric boundary extensions can be imposed.

Before we present examples for $L = 2$, 3, 4, and 5, we will briefly explain why the method for even L in [9] cannot be applied for the case with odd L. In fact, the design of tight frame systems in [9] starts from the existing piecewise linear tight frame

$$\tau_0 = \frac{1}{4}[1,2,1], \tau_1 = \frac{\sqrt{2}}{4}[1,0,-1], \tau_2 = \frac{1}{4}[1,-2,1] \tag{19}$$

as reported in [44]. For any even L, ${}_Lm_0$ is then decomposed as the sum of τ_0 and its double shifted versions while ${}_Lm_1$ is then decomposed as the sum of τ_1 and its double shifted versions. For instance, for $L = 6$, we have

$$\begin{aligned}
\frac{1}{12}[1,2,2,2,2,2,1] &= \frac{1}{12}[1,2,1,0,0,0,0] + \frac{1}{12}[0,0,1,2,1,0,0] + \frac{1}{12}[0,0,0,0,1,2,1],\\
\frac{\sqrt{2}}{12}[1,0,0,0,0,0,-1] &= \frac{\sqrt{2}}{12}[1,0,-1,0,0,0,0] + \frac{\sqrt{2}}{12}[0,0,1,0,-1,0,0] + \frac{\sqrt{2}}{12}[0,0,0,0,1,0,-1].
\end{aligned}$$

Clearly, if L is an odd number, we do not have such a decomposition. We further point out that for even L, the number of high-pass filters for the tight frame system designed in [9] is $\frac{3L}{2} - 1$. The number of high-pass filters for the tight frame system designed in the current paper is $2L - 1$. Moreover, we will see in the next section that the symmetric boundary extension for even L and odd L are completely different.

Example 1. $L = 2$: *The low-pass filter* m_0 *and the three high-pass filters* m_1, m_2, m_3 *are* $m_0 = \frac{1}{4}[1,2,1]$, $m_1 = \frac{1}{4}[1,0,-1]$, $m_2 = \frac{1}{4}[1,0,-1]$, *and* $m_3 = \frac{1}{4}[1,-2,1]$, *respectively. Note that* $m_1 = m_2$, *we can design a tight wavelet frame system with only two high-pass filters. This new system has a low-pass filter* $\tau_0 = m_0$, $\tau_1 = \sqrt{2}m_1$, $\tau_2 = m_3$ *as shown in* (19).

Example 2. $L = 3$: *The low-pass filter* m_0 *and the five high-pass filters* m_1, m_2, m_3, m_4, m_5 *are* $m_0 = \frac{1}{6}[1,2,2,1]$, $m_1 = \frac{1}{6}[1,0,0,-1]$, $m_2 = \frac{\sqrt{6}}{12}[1,1,-1,-1]$, $m_3 = \frac{\sqrt{6}}{12}[1,-1,-1,1]$, $m_4 = \frac{\sqrt{2}}{12}[1,-1,-1,1]$, *and* $m_5 = \frac{\sqrt{2}}{12}[1,-3,3,-1]$, *respectively.*

Example 3. *$L=4$: The low-pass filter m_0 and the seven high-pass filters m_i, $1\le i\le 7$, are*

$$m_0=\tfrac{1}{8}[1,2,2,2,1], m_1=\tfrac{1}{8}[1,0,0,0,-1],$$
$$m_2=\tfrac{\sqrt{2}}{8}\cos(\tfrac{\pi}{8})[1,\sqrt{2},0,-\sqrt{2},-1], m_3=\tfrac{\sqrt{2}}{8}[\cos(\tfrac{\pi}{8}),-\sqrt{2}\sin(\tfrac{\pi}{8}),-2\sin(\tfrac{\pi}{8}),-\sqrt{2}\sin(\tfrac{\pi}{8}),\cos(\tfrac{\pi}{8})],$$
$$m_4=\tfrac{1}{8}[1,0,-2,0,1], m_5=\tfrac{1}{8}[1,-2,0,2,-1],$$
$$m_6=\tfrac{\sqrt{2}}{8}\sin(\tfrac{\pi}{8})[1,-\sqrt{2},0,\sqrt{2},-1], m_7=\tfrac{\sqrt{2}}{8}[\sin(\tfrac{\pi}{8}),-\sqrt{2}\cos(\tfrac{\pi}{8}),2\cos(\tfrac{\pi}{8}),-\sqrt{2}\cos(\tfrac{\pi}{8}),\sin(\tfrac{\pi}{8})].$$

Note that the tight framelet frame designed in [9] is $\tau_0=\frac{1}{8}[1,2,2,2,1]$, $\tau_1=\frac{\sqrt{2}}{8}[1,0,0,0,-1]$, $\tau_2=\frac{1}{8}[-1,2,-2,2,-1]$, $\tau_3=\frac{1}{8}[1,2,0,-2,-1]$, $\tau_4=\frac{\sqrt{2}}{8}[1,0,-2,0,1]$, and $\tau_5=\frac{1}{8}[-1,2,0,-2,1]$. Again we have $\tau_1=\sqrt{2}m_1$.

Example 4. *$L=5$: The low-pass filter m_0 and the nine high-pass filters m_i, $1\le i\le 9$, are*

$$\begin{aligned}
m_0 &= \frac{1}{10}[1,2,2,2,2,1],\\
m_1 &= \frac{1}{10}[1,0,0,0,0,-1],\\
m_2 &= [\frac{\sqrt{2}}{10}\cos\frac{\pi}{10},\frac{\sqrt{2}}{5}\cos\frac{\pi}{10}\cos\frac{\pi}{5},\frac{\sqrt{2}}{10}\cos\frac{3\pi}{10},-\frac{\sqrt{2}}{10}\cos\frac{3\pi}{10},-\frac{\sqrt{2}}{5}\cos\frac{\pi}{10}\cos\frac{\pi}{5},-\frac{\sqrt{2}}{10}\cos\frac{\pi}{10}],\\
m_3 &= [\frac{\sqrt{2}}{10}\cos\frac{\pi}{10},-\frac{\sqrt{2}}{5}\sin\frac{\pi}{10}\sin\frac{\pi}{5},-\frac{\sqrt{2}}{10}\cos\frac{3\pi}{10},-\frac{\sqrt{2}}{10}\cos\frac{3\pi}{10},-\frac{\sqrt{2}}{5}\sin\frac{\pi}{10}\sin\frac{\pi}{5},\frac{\sqrt{2}}{10}\cos\frac{\pi}{10}],\\
m_4 &= [\frac{\sqrt{2}}{10}\cos\frac{\pi}{5},\frac{\sqrt{2}}{5}\cos\frac{\pi}{5}\cos\frac{2\pi}{5},-\frac{\sqrt{2}}{5}\cos^2\frac{\pi}{5},-\frac{\sqrt{2}}{5}\cos^2\frac{\pi}{5},\frac{\sqrt{2}}{5}\cos\frac{\pi}{5}\cos\frac{2\pi}{5},\frac{\sqrt{2}}{10}\cos\frac{\pi}{5}],\\
m_5 &= [\frac{\sqrt{2}}{10}\cos\frac{\pi}{5},-\frac{\sqrt{2}}{5}\sin\frac{\pi}{5}\sin\frac{2\pi}{5},-\frac{\sqrt{2}}{5}\cos^2\frac{3\pi}{10},\frac{\sqrt{2}}{5}\cos^2\frac{3\pi}{10},\frac{\sqrt{2}}{5}\cos\frac{\pi}{5}\cos\frac{2\pi}{5},-\frac{\sqrt{2}}{10}\cos\frac{\pi}{5}],\\
m_6 &= [\frac{\sqrt{2}}{10}\cos\frac{3\pi}{10},-\frac{\sqrt{2}}{5}\sin\frac{\pi}{10}\sin\frac{\pi}{5},-\frac{\sqrt{2}}{10}\cos\frac{\pi}{10},\frac{\sqrt{2}}{10}\cos\frac{\pi}{10},\frac{\sqrt{2}}{5}\sin\frac{\pi}{10}\sin\frac{\pi}{5},-\frac{\sqrt{2}}{10}\cos\frac{3\pi}{10}],\\
m_7 &= [\frac{\sqrt{2}}{10}\cos\frac{3\pi}{10},-\frac{\sqrt{2}}{5}\cos\frac{\pi}{10}\cos\frac{\pi}{5},\frac{\sqrt{2}}{10}\cos\frac{\pi}{10},\frac{\sqrt{2}}{10}\cos\frac{\pi}{10},-\frac{\sqrt{2}}{5}\cos\frac{\pi}{10}\cos\frac{\pi}{5},\frac{\sqrt{2}}{10}\cos\frac{3\pi}{10}],\\
m_8 &= [\frac{\sqrt{2}}{10}\cos\frac{2\pi}{5},-\frac{\sqrt{2}}{5}\sin\frac{\pi}{10}\sin\frac{3\pi}{10},\frac{\sqrt{2}}{5}\sin^2\frac{\pi}{10},\frac{\sqrt{2}}{5}\sin^2\frac{\pi}{10},-\frac{\sqrt{2}}{5}\sin\frac{\pi}{10}\sin\frac{3\pi}{10},\frac{\sqrt{2}}{10}\cos\frac{2\pi}{5}],\\
m_9 &= [\frac{\sqrt{2}}{10}\cos\frac{2\pi}{5},-\frac{\sqrt{2}}{5}\cos\frac{\pi}{10}\cos\frac{3\pi}{10},\frac{\sqrt{2}}{5}\sin^2\frac{2\pi}{5},-\frac{\sqrt{2}}{5}\sin^2\frac{2\pi}{5},\frac{\sqrt{2}}{5}\cos\frac{\pi}{10}\cos\frac{3\pi}{10},-\frac{\sqrt{2}}{10}\cos\frac{2\pi}{5}].
\end{aligned}$$

3.3 Analysis of the Algorithms

Let $m_0, m_1, \ldots m_N$ be the low and high pass filters of a tight framelet system given in the previous section with m_0 being the low-pass filter and m_1 being the high-pass filter defined in (15) for a fixed L. The high resolution image reconstruction without displacement error is essentially to solve v when $m_0 * v$ is given. We describe our algorithms here in the Fourier domain for the one dimensional case. The matrix form of the algorithms in two dimensional case is given in the next section. In the Fourier domain, the problem becomes one of finding $\widehat{v}$ when the function $\widehat{m_0 * v}=\widehat{m}_0\widehat{v}$ is given.

Our tight frame iterative algorithm starts from

$$\sum_{i=0}^{N}\overline{\widehat{m}_i(\omega)}\widehat{m}_i(\omega)=1.$$

Suppose that at step n, we have the nth approximation $\widehat{v}_n$. Then

$$\sum_{i=0}^{N} \overline{\widehat{m}_i} \widehat{m}_i \widehat{v}_n = \widehat{v}_n. \tag{20}$$

Assume that there is no displacement error. Since $\tau_0 \widehat{v} = \widehat{m_0 * v}$ is available, we replace $\widehat{m}_0 \widehat{v}_n$ in (20) by $\widehat{m_0 * v}$ (i.e. $\tau_0 \widehat{v}$) to improve the approximation. By this, we define

$$\widehat{v}_{n+1} = \overline{\widehat{m_0}} \widehat{m_0 * v} + \sum_{i=1}^{N} \overline{\widehat{m}_i} \widehat{m}_i \widehat{v}_n. \tag{21}$$

For the case with displacement errors, the observed image is obtained from the true image v by passing v through the filter $m_0 + 2\epsilon m_1$, see (14). Hence we have $(\widehat{m}_0(\omega) + 2\epsilon \widehat{m}_1(\omega))\widehat{v}$ instead of $\widehat{m}_0 \widehat{v}$. Noting that

$$\overline{\widehat{m_0}(\omega)}(\widehat{m_0}(\omega) + 2\epsilon \widehat{m_1}(\omega) - 2\epsilon \widehat{m}_1(\omega)) + \sum_{i=1}^{N} \overline{\widehat{m}_i(\omega)} \widehat{m}_i(\omega) = 1,$$

and the fact that $(\widehat{m}_0(\omega) + 2\epsilon \widehat{m}_1(\omega))\widehat{v}$ is available, we obtain the following modified algorithm

$$\widehat{v}_{n+1} = \overline{\widehat{m}_0}((\widehat{m}_0 + 2\epsilon \widehat{m}_1)\widehat{v} - 2\epsilon \widehat{m}_1 \widehat{v}_n) + \sum_{i=1}^{N} \overline{\widehat{m}_i} \widehat{m}_i \widehat{v}_n. \tag{22}$$

Essentially, this algorithm uses $\widehat{m}_1 \widehat{v}_n$ to estimate the displacement error $\widehat{m}_1 \widehat{v}$ in $(\widehat{m}_0 + 2\epsilon \widehat{m}_1)\widehat{v}$ which is the available data. The term $(\widehat{m}_0 + 2\epsilon \widehat{m}_1)\widehat{v} - 2\epsilon \widehat{m}_1 \widehat{v}_n$ can be viewed as the approximation of the observed image without displacement errors. By this, we reduce the problem of reconstruction of high-resolution image with the displacement errors to that of the one with no displacement errors. This allows us to use the set of filters derived from the case with no displacement errors. Those filters are symmetric and independent of ϵ.

Proposition 1. *Let m_0, m_1, ... m_N be the low and high pass filters of a tight framelet system derived from the unitary extension principle with m_0 and m_1 being the filters defined in* (15) *for a fixed L. Then, the sequence $\widehat{v}_n$ defined in* (22) *converges to $\widehat{v}$ in $\mathcal{L}^2[-\pi, \pi]$ for any arbitrary $\widehat{v}_0 \in \mathcal{L}^2[-\pi, \pi]$.*

Proof. For an arbitrary $\widehat{v}_0 \in \mathcal{L}^2[-\pi, \pi]$, applying (22), we have

$$\widehat{v}_n - \widehat{v} = \left(\sum_{i=1}^{N} \overline{\widehat{m}_i} \widehat{m}_i - 2\epsilon \overline{\widehat{m}_0} \widehat{m}_1 \right)^n (\widehat{v}_0 - \widehat{v}).$$

Since $\sum_{i=1}^{N} \overline{\widehat{m}_i}(\omega) \widehat{m}_i(\omega)$ is a real number, $2\epsilon \overline{\widehat{m}_0(\omega)} \widehat{m}_1(\omega)$ is a pure imaginary number, and $|\epsilon| < 1/2$, we then have, for every $\omega \in [-\pi, \pi]$,

$$\begin{aligned} |\sum_{i=1}^{N} \overline{\widehat{m}_i(\omega)} \widehat{m}_i(\omega) - 2\epsilon \overline{\widehat{m}_0(\omega)} \widehat{m}_1(\omega))|^2 &= (\sum_{i=1}^{N} \overline{\widehat{m}_i(\omega)} \widehat{m}_i(\omega))^2 + 4\epsilon^2 |\widehat{m}_0(\omega)|^2 |\widehat{m}_1(\omega)|^2 \\ &\leq \sum_{i=0}^{N} \overline{\widehat{m}_i(\omega)} \widehat{m}_i(\omega) = 1. \end{aligned}$$

Furthermore, since

$$|\sum_{i=1}^{N}\overline{\widehat{m}_i(\omega)}\widehat{m}_i(\omega)-2\epsilon\overline{\widehat{m}_0(\omega)}\widehat{m}_1(\omega))|^2$$

only equals to 1 at finitely many points, the inequality

$$|\sum_{i=1}^{N}\overline{\widehat{m}_i(\omega)}\widehat{m}_i(\omega)-2\epsilon\overline{\widehat{m}_0(\omega)}\widehat{m}_1(\omega))|^2<1$$

holds for $\omega\in[-\pi,\pi]$ a.e.. Hence,

$$\left(\sum_{i=1}^{N}\overline{\widehat{m}_i}\widehat{m}_i-2\epsilon\overline{\widehat{m}_0}\widehat{m}_1\right)^n(\widehat{v}_0-\widehat{v})$$

converges to zero for almost every $\omega\in[-\pi,\pi]$. By the Dominated convergence theorem, $\widehat{v}_n$ converges to $\widehat{v}$ in $\mathcal{L}^2$-norm. □

When the observed image contains noise, then v_n has noise brought in from the previous iteration. One then has to apply a denoising procedure at each iteration. Here we consider two different approaches. The first one is similar to the denoising procedure given in [9]. The idea is to decompose the high frequency components $\widehat{m}_i\widehat{v}_n$, $i=1,\ldots N$ via the standard tight framelet decomposition algorithm. This gives a framelet packet decomposition of v_n. Then, applying a framelet denoising algorithm to this decomposition of each $\widehat{m}_i\widehat{v}_n$, $i=1,\ldots,N$ and reconstructing $\widehat{m}_i\widehat{v}_n$, $i=1,\ldots N$ back via the standard reconstruction algorithm leads to a denoising procedure for $\widehat{m}_i\widehat{v}_n$, $i=1,\ldots,N$. The whole denoising procedure is implemented in space (or time) domain instead of Fourier domain. The detailed algorithm is given in Algorithm 1 in the next section.

Another approach is to apply standard Donoho orthonormal wavelet denoising scheme on each v_n before it is used to obtain the next iteration. Although our numerical simulation shows that the denoising scheme mentioned in the last paragraph gives a better performance, this new iteration can be proved to be convergent if the soft threshold (see (32) and (33) for the definitions of soft threshold) is used in the denoising scheme. Indeed, this is a direct corollary of Theorem 3.1 in [15]. For it was proven in [15] that given a converging iteration that solves an inverse problem, the iteration will still be convergent if one adds a soft threshold denoising scheme based on an orthonormal system at each iteration under the assumption that the underlying solution can be represented by the orthonormal system sparsely. Since images can be modeled as piecewise smooth functions that can be sparsely represented by orthonormal wavelet systems, and since our iteration defined in (22) converges, Theorem 3.1 of [15] can be applied to conclude that this new algorithm converges. In fact, Theorem 3.1 of [15] was stated in a more general setting and the interested reader should consult [15] for the details. The details of implementation of this algorithm is given in Algorithm 2.

4 Matrix Form

Setting $\ell=0$ in (18) yields

$$\sum_{q=0}^{1}\sum_{p=0}^{L-1}|\widehat{m}_{2p+q}(\omega)|^2=1. \qquad (23)$$

For any signal u, we have

$$\sum_{q=0}^{1}\sum_{p=0}^{L-1}|\widehat{m}_{2p+q}(\omega)|^2\widehat{u}(\omega)=\widehat{u}(\omega).$$

In the time domain, the above identity is equivalent to

$$\sum_{q=0}^{1}\sum_{p=0}^{L-1}(\underline{m}_{2p+q}*m_{2p+q}*u)(n)=u(n)\quad\forall n\in\mathbb{Z},\tag{24}$$

where $\underline{m}_{2p+q}(k)=m_{2p+q}(-k)$ for all k. Our purpose is to construct, under certain symmetric boundary conditions, $N\times N$ matrices $\mathbf{T}_k$ and $\underline{\mathbf{T}}_k$, $k=0,\ldots,2L-1$, such that

$$\sum_{q=0}^{1}\sum_{p=0}^{L-1}\underline{\mathbf{T}}_{2p+q}\mathbf{T}_{2p+q}u=u\tag{25}$$

for any vector u. This is equivalent to

$$\sum_{q=0}^{1}\sum_{p=0}^{L-1}\underline{\mathbf{T}}_{2p+q}\mathbf{T}_{2p+q}=\mathbf{I}\tag{26}$$

To construct the matrices $\mathbf{T}_k$ and $\underline{\mathbf{T}}_k$, for $k=0,\ldots,2L-1$, we consider two separate cases: L is even and L is odd. The detailed formulation of the matrices $\mathbf{T}_k$ and $\underline{\mathbf{T}}_k$ is given in [10].

4.1 L is even

If L is even, the $N\times N$ matrices

$$\underline{\mathbf{T}}_k=\begin{cases}\text{Toeplitz}(\mathbf{a},\mathbf{b})+\text{PseudoHankel}(\mathbf{b},\mathbf{a}), & \text{when } k=2p+q \text{ and } p+q \text{ is even,}\\ \text{Toeplitz}(\mathbf{a},\mathbf{b})+\text{PseudoHankel}(-\mathbf{b},-\mathbf{a}), & \text{when } k=2p+q \text{ and } p+q \text{ is odd,}\end{cases}$$

for all $k=0,\ldots,2L-1$, and

$$\mathbf{a}=[\underline{m}_k(0),\cdots,\underline{m}_k(-L/2),0,\cdots,0]^t\quad\text{and}\quad\mathbf{b}=[\underline{m}_k(0),\cdots,\underline{m}_k(L/2),0,\cdots,0]^t.$$

Similarly, the $N\times N$ matrices

$$\mathbf{T}_k=\text{Toeplitz}(\mathbf{a},\mathbf{b})+\text{PseudoHankel}(\mathbf{b},\mathbf{a})$$

for all $k=0,\ldots,2L-1$ with

$$\mathbf{a}=[m_k(0),\cdots,m_k(-L/2),0,\cdots,0]^t\quad\text{and}\quad\mathbf{b}=[m_k(0),\cdots,m_k(L/2),0,\cdots,0]^t.$$

4.2 L is odd

If L is odd, the $N\times N$ matrices

$$\underline{\mathbf{T}}_k=\begin{cases}\text{Toeplitz}(\mathbf{a},\mathbf{b})+\text{PseudoHankel}(\mathbf{b},\mathbf{0})+\text{Hankel}(\mathbf{0},\mathbf{a}),\\ \qquad\qquad\text{when } k=2p+q \text{ and } p+q \text{ is even,}\\ \text{Toeplitz}(\mathbf{a},\mathbf{b})+\text{PseudoHankel}(-\mathbf{b},\mathbf{0})+\text{Hankel}(\mathbf{0},-\mathbf{a}),\\ \qquad\qquad\text{when } k=2p+q \text{ and } p+q \text{ is odd,}\end{cases}$$

for all $k = 0, \ldots, 2L-1$ with

$$\mathbf{a} = [\underline{m}_k(0), \cdots, \underline{m}_k(-(L+1)/2), 0, \cdots, 0]^t \quad \text{and} \quad \mathbf{b} = [\underline{m}_k(0), \cdots, \underline{m}_k((L-1)/2), 0, \cdots, 0]^t.$$

Similarly, the $N \times N$ matrices

$$\mathbf{T}_k = \text{Toeplitz}(\mathbf{a}, \mathbf{b}) + \text{PseudoHankel}(\mathbf{b}, \mathbf{0}) + \text{Hankel}(\mathbf{0}, \mathbf{a}),$$

for all $k = 0, \ldots, 2L-1$ with

$$\mathbf{a} = [m_k(0), \cdots, m_k(-(L-1)/2), 0, \cdots, 0]^t \quad \text{and} \quad \mathbf{b} = [m_k(0), \cdots, m_k((L+1)/2), 0, \cdots, 0]^t.$$

5 Algorithms

For any number $L \geq 2$, the $M_1 \times M_1$ matrices $\mathbf{T}_k$ and $\underline{\mathbf{T}}_k$ in (25) are denoted by $\mathbf{T}_k^x$ and $\underline{\mathbf{T}}_k^x$, respectively; the $M_2 \times M_2$ matrices $\mathbf{T}_k$ and $\underline{\mathbf{T}}_k$ in (25) are denoted by $\mathbf{T}_k^y$ and $\underline{\mathbf{T}}_k^y$, respectively. We have

$$\sum_{k=0}^{2L-1} \underline{\mathbf{T}}_k^x \mathbf{T}_k^x = \mathbf{I}_{M_1} \quad \text{and} \quad \sum_{k=0}^{2L-1} \underline{\mathbf{T}}_k^y \mathbf{T}_k^y = \mathbf{I}_{M_2}.$$

This leads to

$$\sum_{p,q=0}^{2L-1} \underline{\mathbf{T}}_{p,q} \mathbf{T}_{p,q} = \mathbf{I}_{M_1 \times M_2}, \tag{27}$$

where $\mathbf{T}_{p,q} = \mathbf{T}_q^y \otimes \mathbf{T}_p^x$ and $\underline{\mathbf{T}}_{p,q} = \underline{\mathbf{T}}_q^y \otimes \underline{\mathbf{T}}_p^x$. Obviously, $\mathbf{T}_{0,0} = \mathbf{H}(\mathbf{0}, \mathbf{0})$.

Recalling (14), we have

$$\mathbf{H}^x(\epsilon_{\ell_1,\ell_2}^x) = \mathbf{T}_0^x + 2\epsilon_{\ell_1,\ell_2}^x \mathbf{T}_1^x \quad \text{and} \quad \mathbf{H}^y(\epsilon_{\ell_1,\ell_2}^y) = \mathbf{T}_0^y + 2\epsilon_{\ell_1,\ell_2}^y \mathbf{T}_1^y.$$

Therefore, the blurring matrix with displacement errors, i.e. $\mathbf{H}(\boldsymbol{\epsilon}^x, \boldsymbol{\epsilon}^y)$ in (8), can be expressed as the sum of the blurring with no displacement $\mathbf{H}(\mathbf{0}, \mathbf{0})$ together with the matrices $\mathbf{T}_{1,0}$, $\mathbf{T}_{0,1}$, $\mathbf{T}_{1,1}$. More precisely,

$$\mathbf{H}_{0,0}(\epsilon_{\ell_1,\ell_2}^x, \epsilon_{\ell_1,\ell_2}^y) = \mathbf{T}_{0,0} + 2\epsilon_{\ell_1,\ell_2}^x \mathbf{T}_{1,0} + 2\epsilon_{\ell_1,\ell_2}^y \mathbf{T}_{0,1} + 4\epsilon_{\ell_1,\ell_2}^x \epsilon_{\ell_1,\ell_2}^y \mathbf{T}_{1,1}. \tag{28}$$

By definition (9), $\sum_{\ell_1=0}^{L-1} \sum_{\ell_2=0}^{L-1} \mathbf{D}_{\ell_1,\ell_2} = \mathbf{I}_{M_1 \times M_2}$. Hence we get

$$\mathbf{H}(\boldsymbol{\epsilon}^x, \boldsymbol{\epsilon}^y) = \mathbf{T}_{0,0} + 2\mathbf{S}(\boldsymbol{\epsilon}^x)\mathbf{T}_{1,0} + 2\mathbf{S}(\boldsymbol{\epsilon}^y)\mathbf{T}_{0,1} + 4\mathbf{S}(\boldsymbol{\epsilon}^{xy})\mathbf{T}_{1,1} \tag{29}$$

where $\boldsymbol{\epsilon}^{xy} = [\epsilon_{\ell_1,\ell_2}^x \cdot \epsilon_{\ell_1,\ell_2}^y]_{\ell_1,\ell_2=0}^{L-1}$ and $\mathbf{S}(\boldsymbol{\epsilon}) = \sum_{\ell_1=0}^{L-1} \sum_{\ell_2=0}^{L-1} \epsilon_{\ell_1,\ell_2} \cdot \mathbf{D}_{\ell_1,\ell_2}$.

Multiplying $\mathbf{f}$ to both sides of (29) leads to

$$\mathbf{H}(\boldsymbol{\epsilon}^x, \boldsymbol{\epsilon}^y)\mathbf{f} = \mathbf{T}_{0,0}\mathbf{f} + 2\mathbf{S}(\boldsymbol{\epsilon}^x)\mathbf{T}_{1,0}\mathbf{f} + 2\mathbf{S}(\boldsymbol{\epsilon}^y)\mathbf{T}_{0,1}\mathbf{f} + 4\mathbf{S}(\boldsymbol{\epsilon}^{xy})\mathbf{T}_{1,1}\mathbf{f}.$$

This equation says that the observed high-resolution image $\mathbf{g} = \mathbf{H}(\boldsymbol{\epsilon}^x, \boldsymbol{\epsilon}^y)\mathbf{f}$ is the sum of $\mathbf{T}_{0,0}\mathbf{f}$ (which equals to $\mathbf{H}(\mathbf{0}, \mathbf{0})\mathbf{f}$, the observed high-resolution image without any displacement errors), and three high-frequency images. Conversely, the observed image in the case with no displacement errors can be represented by the observed images with displacement errors:

$$\mathbf{H}(\mathbf{0}, \mathbf{0})\mathbf{f} = \mathbf{T}_{0,0}\mathbf{f} = \mathbf{H}(\boldsymbol{\epsilon}^x, \boldsymbol{\epsilon}^y)\mathbf{f} - [2\mathbf{S}(\boldsymbol{\epsilon}^x)\mathbf{T}_{1,0}\mathbf{f} + 2\mathbf{S}(\boldsymbol{\epsilon}^y)\mathbf{T}_{0,1}\mathbf{f} + 4\mathbf{S}(\boldsymbol{\epsilon}^{xy})\mathbf{T}_{1,1}\mathbf{f}]. \tag{30}$$

Thus with the matrices $\mathbf{T}_{1,0}$, $\mathbf{T}_{0,1}$, and $\mathbf{T}_{1,1}$, we can always approximate $\mathbf{H}(\mathbf{0}, \mathbf{0})\mathbf{f}$ independent of the displacement errors. In other words, unlike the work in [8], the tight system we used is fixed and can be used for all displacement errors.

Two algorithms will be proposed in the following subsections.

5.1 Algorithm 1

This algorithm is essentially the same as the one proposed in [9].

Algorithm 1.

1. *Choose an initial guess* $\mathbf{f}_0$*;*
2. *Iterate on* n *until convergence;*
   (a) *compute all framelet coefficients* $\mathbf{T}_{p,q}\mathbf{f}_n$ *for* $(p,q) \neq (0,0)$ *for* $p,q = 0,\ldots,2L-1$.
   (b) *estimate the observed image* $\widetilde{\mathbf{g}}$ *according to* (30)*:*
   $$\widetilde{\mathbf{g}} = \mathbf{g} - \left(2\mathbf{S}(\boldsymbol{\epsilon}^x)\mathbf{T}_{1,0} + 2\mathbf{S}(\boldsymbol{\epsilon}^y)\mathbf{T}_{0,1} + 4\mathbf{S}(\boldsymbol{\epsilon}^{xy})\mathbf{T}_{1,1}\right)\mathbf{f}_n.$$
   (c) *denoise framelet coefficients* $\mathbf{T}_{p,q}\mathbf{f}_n$*,* $(p,q) \neq (0,0)$*, by the denoising operator* $\mathcal{D}$ *(we will define it later).*
   (d) *reconstruct an image* $\mathbf{f}_{n+1}$ *from the estimated observed image* $\widetilde{\mathbf{g}}$ *and denoised wavelet coefficients* $\mathcal{D}(\mathbf{T}_{p,q}\mathbf{f}_n)$*, i.e.*
   $$\mathbf{f}_{n+1} \quad = \quad \underline{\mathbf{T}}_{0,0}\widetilde{\mathbf{g}} + \sum_{\substack{p,q=0 \\ (p,q)\neq(0,0)}}^{2L-1} \underline{\mathbf{T}}_{p,q}\mathcal{D}(\mathbf{T}_{p,q}\mathbf{f}_n). \tag{31}$$

One of the major points of our algorithm is that Donoho's denoising operator $\mathcal{D}$ can be built into the iteration procedure. Although orthogonal and bi-orthogonal wavelets can be used as the denoising operator $\mathcal{D}$, we insist in using the constructed tight framelets with $L = 2$ for Algorithm 1, since it is simple and efficient. To this end, the matrices $\mathbf{W}_{p,q}$ and $\underline{\mathbf{W}}_{p,q}$ correspond to the matrices $\mathbf{T}_{p,q}$ and $\underline{\mathbf{T}}_{p,q}$ in (27) with $L = 2$. The denoising operator for two-dimensional images can be simply written as

$$\mathcal{D}(\mathbf{f}) = (\underline{\mathbf{W}}_{0,0})^Q(\mathbf{W}_{0,0})^Q\mathbf{f} + \sum_{q=0}^{Q-1}(\underline{\mathbf{W}}_{0,0})^q \sum_{\substack{r,s=0 \\ (r,s)\neq(0,0)}}^{3} \underline{\mathbf{W}}_{r,s}\mathcal{T}_\lambda(\mathbf{W}_{r,s}\mathbf{W}_{0,0}^q\mathbf{f}), \tag{32}$$

where Q is the number of levels used in the decomposition. The operator $\mathcal{T}_\lambda$ is the thresholding operator defined in [19, 18]. More precisely, for a given λ, let

$$\mathcal{T}_\lambda((x_1,\ldots,x_l,\ldots)^t) = (t_\lambda(x_1),\ldots,t_\lambda(x_l),\ldots)^t, \tag{33}$$

where the thresholding function t_λ is either (i) $t_\lambda(x) = x\chi_{|x|>\lambda}$, referred to as the *hard threshold*, or (ii) $t_\lambda(x) = \mathrm{sgn}(x)\max(|x|-\lambda, 0)$, the *soft threshold*. A typical choice for λ is $\lambda = \sigma\sqrt{2\log(M_1M_2)}$ where σ is the variance of the Gaussian noise in the signal $\mathbf{f}$ estimated numerically by the method given in [19]. We use the hard threshold in Algorithm 1.

The computational complexity of each iteration in Algorithm 1 is $O(M_1M_2\log(M_1M_2))$. This complexity is also proportional to $4L^2-1$, the number of matrices $\mathbf{T}_{p,q}$, $(p,q) \neq (0,0)$. Therefore, to reduce the computational complexity at each iteration, one way is to construct a tight frame system of $\mathcal{L}^2(\mathbb{R})$ with the smallest number of tight framelets as possible. Of course, ${}_Lm_0$ and ${}_Lm_1$ must be the low-pass filter and one of the high-pass filters associated with this tight frame system.

5.2 Algorithm 2

This algorithm is new and has not been proposed before.

Algorithm 2.

1. *Choose an initial guess* $\mathbf{f}_0$*;*
2. *Iterate on* n *until convergence;*
   (a) *denoise the image* $\mathbf{f}_n$ *by the denoising operator* $\mathcal{D}$ *defined in* (32)*, the resulting image is*
   $$\widetilde{\mathbf{f}}_n = \mathcal{D}(\mathbf{f}_n).$$
   (b) *estimate the observed image* $\widetilde{\mathbf{g}}$ *according to* (30)*:*
   $$\widetilde{\mathbf{g}} = \mathbf{g} - \left(2\mathbf{S}(\boldsymbol{\epsilon}^x)\mathbf{T}_{1,0} + 2\mathbf{S}(\boldsymbol{\epsilon}^y)\mathbf{T}_{0,1} + 4\mathbf{S}(\boldsymbol{\epsilon}^{xy})\mathbf{T}_{1,1}\right)\widetilde{\mathbf{f}}_n.$$
   (c) *reconstruct an image* $\mathbf{f}_{n+1}$ *from the estimated observed image* $\widetilde{\mathbf{g}}$ *and* $\widetilde{\mathbf{f}}_n$*, i.e.*
   $$\mathbf{f}_{n+1} = \underline{\mathbf{T}}_{0,0}\widetilde{\mathbf{g}} + (\mathbf{I} - \underline{\mathbf{T}}_{0,0}\mathbf{T}_{0,0})\widetilde{\mathbf{f}}_n.$$

As indicated at the end of Section 3, Algorithm 2 will converge if orthogonal wavelets are used in the denoising operator $\mathcal{D}$. However, here we use linear tight framelets instead of the orthogonal wavelets in the denoising operator $\mathcal{D}$ because the results with tight framelets are much better than that with orthogonal wavelets. We use the soft threshold in Algorithm 2.

The computational complexity of each iteration in Algorithm 2 is still $O(M_1M_2\log(M_1M_2))$. Unlike Algorithm 1, this complexity is independent of the number of matrices $\mathbf{T}_{p,q}$, $(p,q) \neq (0,0)$. Therefore, comparing with Algorithm 1, this new algorithm significantly reduces the computational cost.

6 Numerical Experiments

In this section, we implement our tight framelet based high-resolution image reconstruction algorithm developed in previous sections. We evaluate our method using the peak signal-to-noise ratio (PSNR) which compares the reconstructed image $\mathbf{f}_c$ with the original image $\mathbf{f}$. It is defined by PSNR $= 10\log_{10}\frac{255^2 M_1M_2}{\|\mathbf{f}-\mathbf{f}_c\|_2^2}$, where the size of the restored images is $M_1 \times M_2$. We use the "Bridge", "Boat", and "Baboon" images of size 260×260 as the original images in our numerical tests, see Figure 1. We use $Q = 1$ in (32) and stop the iteration process when the reconstructed HR image achieves the highest PSNR value. The maximum number of iteration is set to 200.

For any $L \times L$ sensor array, the displacement errors matrices $\boldsymbol{\epsilon}^x$ and $\boldsymbol{\epsilon}^y$ are generated by the following three MATLAB commands

$$rand('seed', 100); \boldsymbol{\epsilon}^x = 0.99 * (rand(L) - 0.5); \boldsymbol{\epsilon}^y = 0.99 * (rand(L) - 0.5);$$

The $L \times L$ sensor array with displacement errors $\boldsymbol{\epsilon}^x$ and $\boldsymbol{\epsilon}^y$ produces L^2's LR images.

For 2×2, 3×3, 4×4, and 5×5 sensor arrays, the tight framelets we used are designed in Examples 1, 2, 3, and 4, respectively. Figures 2–3 give the PSNR values of the reconstructed images at each iteration for the "Boat" image (left column), the "Bridge" image (middle column), and the "Baboon" image (right column) for sensor arrays of different sizes by using Algorithm 1 and Algorithm 2, respectively. Figures 4–7 depict the reconstructed HR images with noise at SNR = 30

Figure 1: Original “Boat” image (left); original “Bridge” image (middle); original “Baboon” image (right).

dB. We see that we can obtain quite good images even for L as large as 5. In terms of PSNR values, Algorithm 1 is better than Algorithm 2.

For comparison between the wavelet (or framelet) approach with Tikhonov approach, we refer the readers to [7, 8, 9], where the numerical results have consistently shown that the wavelet approach always outperforms the Tikhonov approach.

7 Conclusions

In this paper, we continue on our early work in [9]. First, we designed a tight wavelet frame system with ${}_Lm_0$ as its low-pass filter and ${}_Lm_1$ as one of its high-pass filters for any integer $L \geq 2$. The filters are symmetric or antisymmetric so that the proposed tight frame algorithms work for symmetric boundary conditions. Secondly, an analysis of the convergence of the algorithm in [9] is given. It is shown that the algorithm converges when there is no noise in the given data. When the data has noise, a denoising scheme should be built in to remove noise. The algorithm can be proven to converge for some denoising scheme, e.g. the one given in Algorithm 2. In our future works, we will construct a tight frame system which has as small number of tight framelets as possible in order to reduce the computational complexity of our proposed Algorithm 1. We will also develop an efficient denoising scheme, since it is critical for getting good reconstructed images and proving the convergence of the algorithm.

Acknowledgments

The authors would like to thank the referees for providing us constructive comments and insightful suggestions.

References

[1] S. Borman and R. Stevenson. Super-resolution from image sequences—a review. In *Proceedings of the 1998 Midwest Symposium on Circuits and Syatems*, volume 5, 1998.

[2] N. Bose and K. Boo. High-resolution image reconstruction with multisensors. *International Journal of Imaging Systems and Technology*, 9:294–304, 1998.

[3] N. Bose, H. Kim, and H. Valenzuela. Recursive total least squares algorithm for image reconstruction from noisy undersampled frames. *Multidimensional Systems and Signal Processing*, 4(3):253–268, 1993.

[4] N. Bose, S. Lertrattanapanich, and J. Koo. Advances in superresolution using the L-curve. *Proc. Int. Symp. Circuits and Systems*, Vol II, pp. 433-436, Sydney, NSW, Australia, 2001.

[5] C. Brislawn. Classification of nonexpansive symmetric extension transforms for multirate filter banks. *Applied and Computational Harmonic Analysis*, 3:337–357, 1996.

[6] R. Chan, T. Chan, L. Shen, and Z. Shen. A wavelet method for high-resolution image reconstruction with displacement errors. In *Proceedings of the 2001 International Symposium on Intelligent Multimedia, Video and Speech Processing*, pages 24–27, Hong Kong, 2001.

[7] R. Chan, T. Chan, L. Shen, and Z. Shen. Wavelet algorithms for high-resolution image reconstruction. *SIAM Journal on Scientific Computing*, 24(4):1408–1432, 2003.

[8] R. Chan, T. Chan, L. Shen, and Z. Shen. Wavelet deblurring algorithms for spatially varying blur from high-resolution image reconstruction. *Linear Algebra and its Applications*, 366:139–155, 2003.

[9] R. Chan, S. D. Riemenschneider, L. Shen, and Z. Shen. Tight frame: The efficient way for high-resolution image reconstruction. *Applied and Computational Harmonic Analysis*, to appear.

[10] R. Chan, S. D. Riemenschneider, L. Shen, and Z. Shen. High-resolution image reconstruction with displacement errors: A framelet approach. Research Report #CUHK-2004-04 (311), Department of Mathematics, The Chinese University of Hong Kang, 2004.

[11] C. Chui and W. He. Compactly supported tight frames associated with refinable functions. *Applied and Computational Harmonic Analysis*, 8:293–319, 2000.

[12] C. Chui, W. He, and J. Stockler. Compactly supported tight and sibling frames with maximum vanishing moments. *Applied and Computation Harmonic Analysis*, 13:224–262, 2002.

[13] I. Daubechies. Orthogonal bases of compactly supported wavelets. *Comm. Pure and Applied Math.*, 41:909–996, 1988.

[14] I. Daubechies. *Ten Lectures on Wavelets*, volume 61 of *CBMS Conference Series in Applied Mathematics*. SIAM, Philadelphia, 1992.

[15] I. Daubechies, M. Defrise and C. De Mol, “An iterative thresholding algorithm for linear inverse problems with a sparsity constraint”, Preprint, 2003.

[16] I. Daubechies, B. Han, A. Ron, and Z. Shen. Framelets: MRA-based constructions of wavelet frames. *Applied and Computation Harmonic Analysis*, 14:1–46, 2003.

[17] C. de Boor, R. DeVore, and A. Ron. On the construction of multivariate (pre)-wavelets. *Constr. Approx.*, 9:123–166, 1993.

[18] D. Donoho. De-noising by soft-thresholding. *IEEE Transactions on Information Theory*, 41:613–627, 1995.

[19] D. Donoho and I. Johnstone. Ideal spatial adaptation by wavelet shrinkage. *Biometrika*, 81:425–455, 1994.

[20] M. Elad and A. Feuer. Restoration of a single superresolution image from several blurred, noisy and undersampled measured images. *IEEE Transactions on Image Processing*, 6:1646–1658, Dec. 1997.

[21] M. Elad and A. Feuer. Superresolution restoration of an image sequence: adaptive filtering approach. *IEEE Transactions on Image Processing*, 8(3):387–395, Mar. 1999.

[22] M. Elad and Y. Hel-Or. A fast super-resolution reconstruction algorithm for pure translational motion and common space-invariant blur. *IEEE Transactions on Image Processing*, 10(8):1187–1193, Aug. 2001.

[23] B. Han. On dual wavelet tight frames. *Applied and Computational Harmonic Analysis*, 4:380–413, 1997.

[24] R. Hardie, K. Barnard, and E. Armstrong. Joint MAP registration and high-resolution image estimation using a sequence of undersampled images. *IEEE Trans. on Image Processing*, 6:1621–1633, 1997.

[25] M. Hong, M. Kang, and A. Katsaggelos. An iterative weighted regularized algorithm for improving the resolution of video sequences. In *IEEE International Conference On Image Processing*, 1997.

[26] T. Huang and R. Tsay. Multiple frame image restoration and registration. In T. S. Huang, editor, *Advances in Computer Vision and Image Processing*, volume 1, pages 317–339, Greenwich, CT: JAI, 1984.

[27] M. Irani and S. Peleg. Improving resolution by image registration. *CVGIP: Graphical Models and Image Processing*, 53:231–239, May 1991.

[28] M. Irani and S. Peleg. Motion analysis for image enhancement: resolution, occlusion, and transparency. *Journal of Visual Communication and Image Representation*, 4:324–335, Dec. 1993.

[29] R. Jia and Z. Shen. Multiresolution and wavelets. *Proceedings of the Edinburgh Mathematical Society*, 37:271–300, 1994.

[30] S. P. Kim, N. K. Bose, and H. M. Vakenzuela. Recursive reconstruction of high resolution image from noisy undersampled multiframes. *IEEE Transactions on Acoustics, Speech, and Signal Processing*, 38:1013–1027, June 1990.

[31] T. Komatsu, K. Aizawa, T. Igarashi, and T. Saito. Signal-processing based method for acquiring very high resolution image with multiple cameras and its theoretical analysis. *IEE Proceedings: Communications, Speech and Vision*, 140(1):19–25, Feb 1993.

[32] S. Lertrattanapanich and N. K. Bose. High resolution image formation from low resolution frames using Delaunay triangulation. *IEEE Transactions on Image Processing*, 11(12):1427–1441, 2002.

[33] R. Molina, M. Vega, J. Abad, and A. Katsaggelos. Parameter estimation in Bayesian high-resolution image reconstruction with multisensors. Technical report, Oct. 2002.

[34] M. Ng and N. Bose. Mathematical analysis of super-resolution methodology. *IEEE Signal Processing Magazine*, pages 62–74, May 2003.

[35] M. Ng, R. Chan, T. Chan, and A. Yip. Cosine transform preconditioners for high resolution image reconstruction. *Linear Algebra and its Applications*, 316:89–104, 2000.

[36] M. Ng, R. Chan, and W. Tang. A fast algorithm for deblurring models with Neumann boundary conditions. *SIAM Journal on Scientific Computing*, 21:851–866, 2000.

[37] M. Ng and A. Yip. A fast MAP algorithm for high-resolution image reconstruction with multisensors. *Multidimensional Systems and Signal Processing*, 12:143–164, 2001.

[38] M. K. Ng and N. Bose. Analysis of displacement errors in high-resolution image reconstruction with multisensors. *IEEE Trans. on Circuits and Systems—I: Fundamental Theory and Applications*, 49(6):806–813, 2002.

[39] M. K. Ng, J. Koo, and N. Bose. Constrained total least squares computations for high resolution image reconstruction with multisensors. *International Journal of Imaging Systems and Technology*, 12:35–42, 2002.

[40] N. Nguyen and P. Milanfar. An efficient wavelet-based algorithm for image superresolution. *IEEE International Conference On Image Processing*, 6:351–354, 2000.

[41] N. Nguyen and P. Milanfar. A wavelet-based interpolation-restoration method for superresolutio. *IEEE Trans. on Circuits, Systems, and Signal Processing*, 19(4):321–338, 2000.

[42] N. Nguyen, P. Milanfar, and G. Golub. A computationally efficient superresolution image reconstruction algorithm. *IEEE Trans. on Image Processing*, 10:573–583, 2001.

[43] A. Papoulis. Generalized sampling expansion. *IEEE Transactions on Circuits and Systems*, 24:652–654, 1977.

[44] A. Ron and Z. Shen. Affine system in $L_2(\mathbb{R}^d)$: the analysis of the analysis operator. *Journal Func. Anal.*, 148:408–447, 1997.

[45] R. Schultz and R. Stevenson. Extraction of high-resolution frames from video sequences. *IEEE Transactions on Image Processing*, 5:996–1011, June 1996.

[46] L. Shen and Q. Sun. Bi-orthogonal wavelet system for high-resolution image reconstruction. *IEEE Transactions on Signal Processing*, July 2004.

[47] H. Stark and P. Oskoui. High resolution image recovery from image-plane arrays, using convex projections. *J. Opt. Soc. Amer.*, 6:1715–1726, 1989.

[48] A. Tekalp. *Digital Video Processing*. Prentice-Hall, 1995.

[49] A. Tekalp, T. Ozkan, and M. Sezan. High resolution image reconstruction from low-resolution image sequences, and space varying image restoration. In *IEEE Int. Conf. Acoustics, Speech, Signal Processing*, volume 3, pages 169–172, San Francisco, CA, Mar. 1992.

[50] H. Ur and D. Gross. Improved resolution from subpixel shifted pictures. *CVGIP: Graphical Vision and Image Processing*, 54(2):181–186, 1992.

[51] L. Yen. On nonuniform sampling of bandwidth limited signals. *IRE Trans. Circuits Theory*, 3:251–257, 1956.

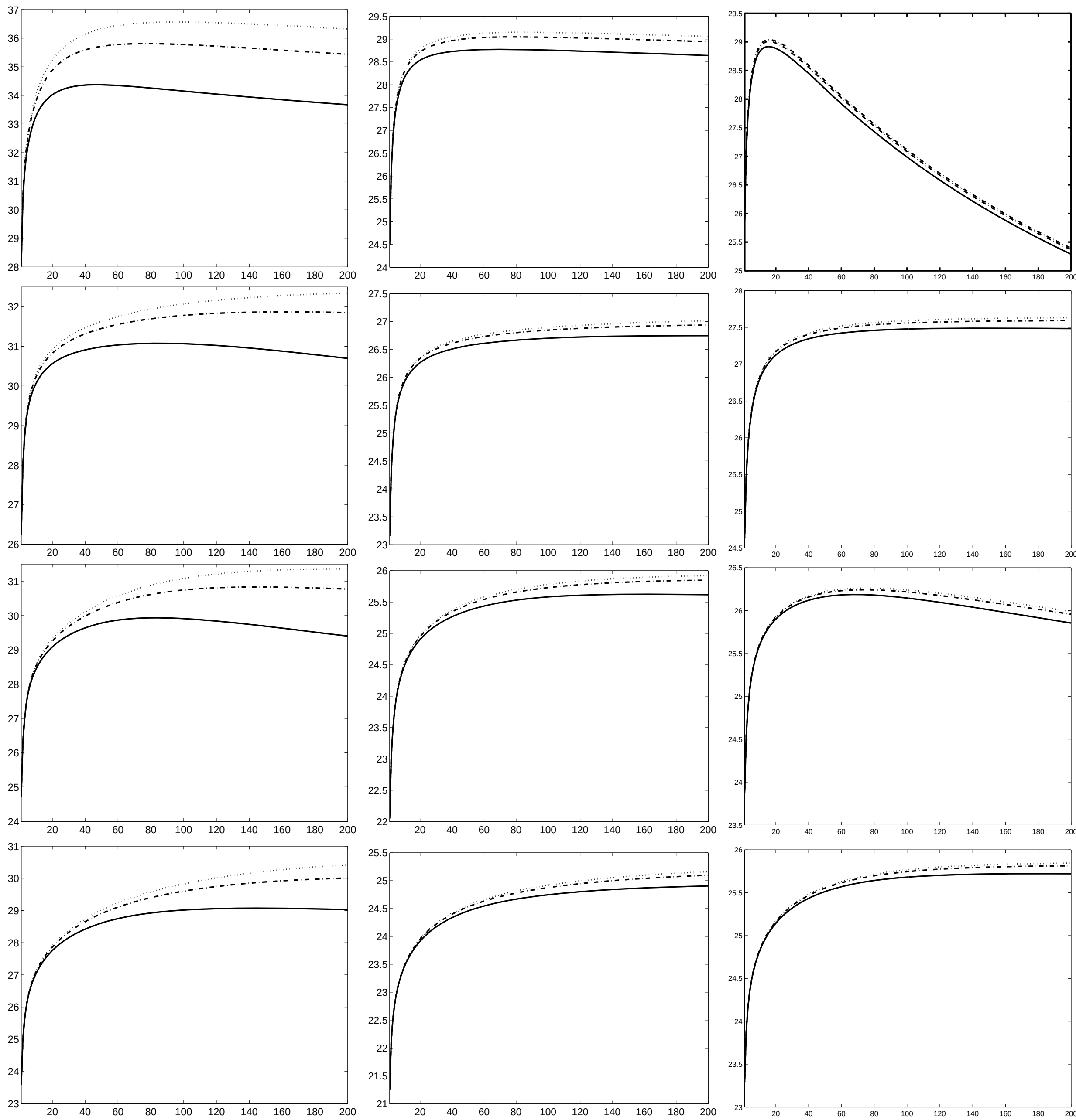

Figure 2: PSNR values at each iteration for "Boat" (left), "Bridge" (middle) and "Baboon" (right) images with 2×2, 3×3, 4×4, and 5×5 (from top to bottom) using Algorithm 1. Solid, dashdot, and dotted lines denote the case where the observed HR images are corrupted with Gaussian white noise at noise level $\mathrm{SNR} = 20$, 30, and 40 respectively.

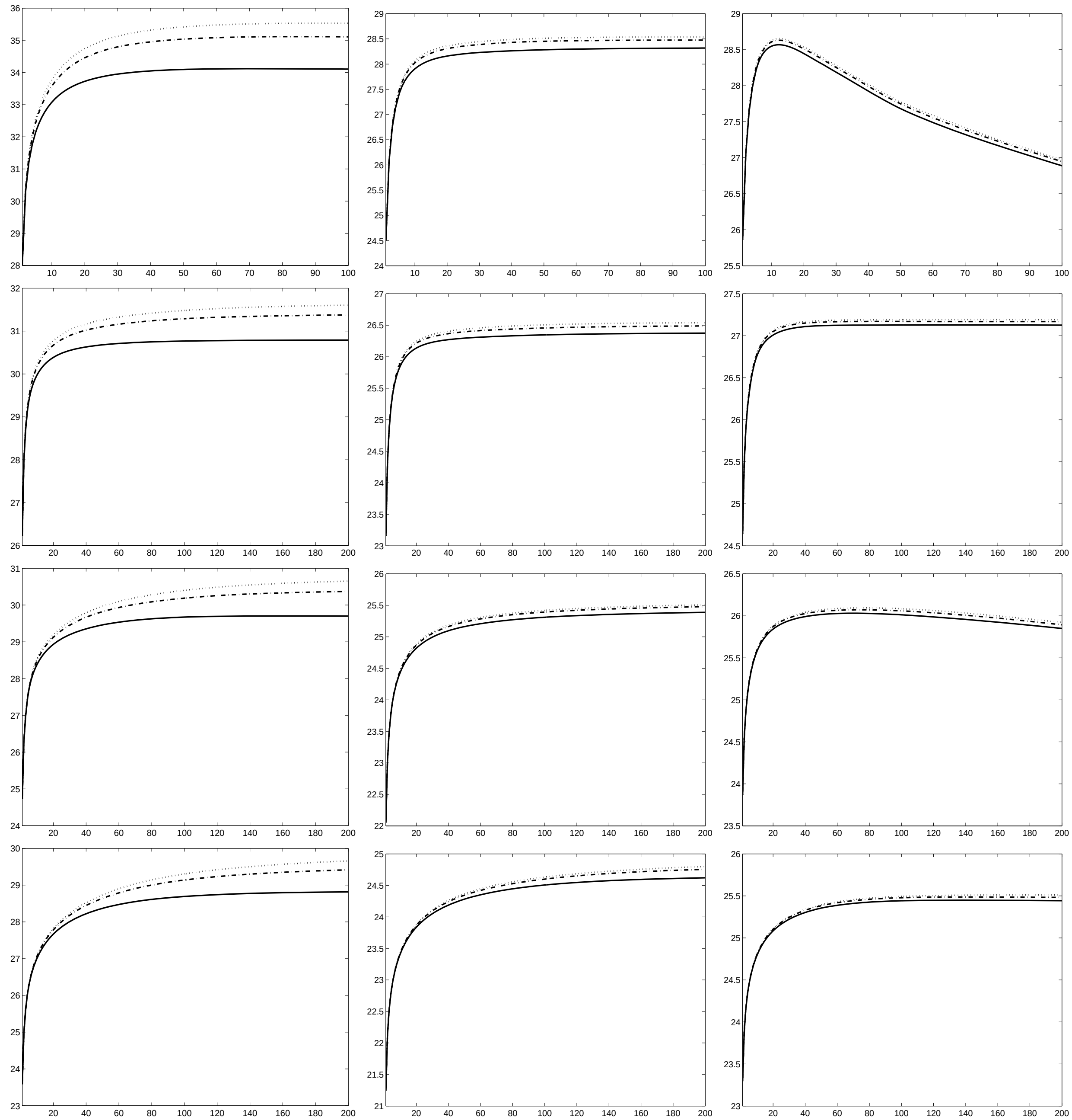

Figure 3: PSNR values at each iteration for "Boat" (left), "Bridge" (middle) and "Baboon" (right) images with 2×2, 3×3, 4×4, and 5×5 (from top to bottom) using Algorithm 2. Solid, dashdot, and dotted lines denote the case where the observed HR images are corrupted with Gaussian white noise at noise level SNR $= 20$, 30, and 40 respectively.

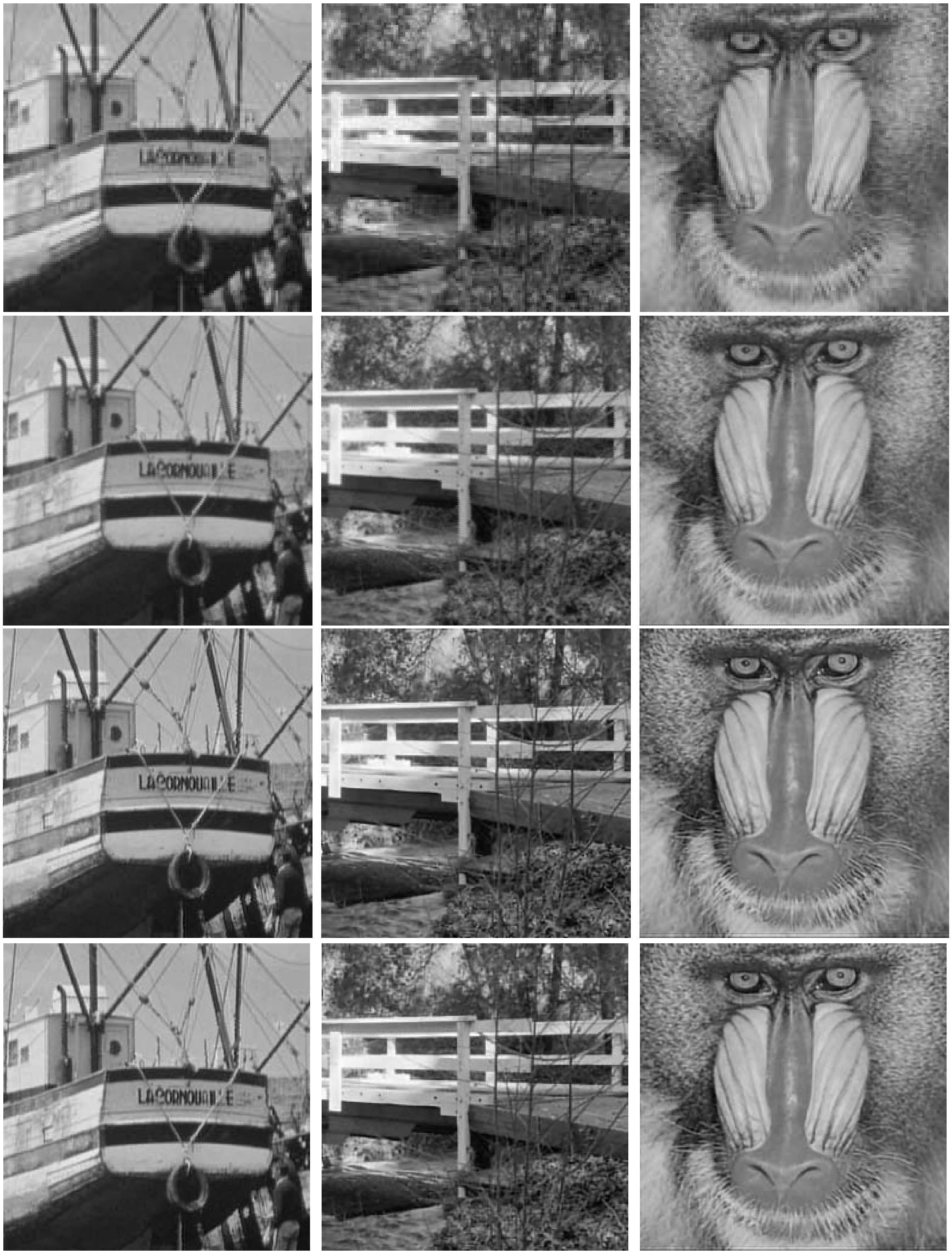

Figure 4: From top to bottom, the $(0, 0)$-th LR images, the observed HR images, and the reconstructed HR images for 2×2 sensor array. The reconstructed HR "Boat" image, "Bridge" image, and "Baboon" image by using Algorithm 1 (the third row) have PSNR = 35.81 dB, 29.05 dB, and 29.01 dB respectively. The reconstructed HR "Boat" image, "Bridge" image, and "Baboon" image by using Algorithm 2 (the forth row) have PSNR = 35.11 dB, 28.48 dB, and 28.63 dB respectively.

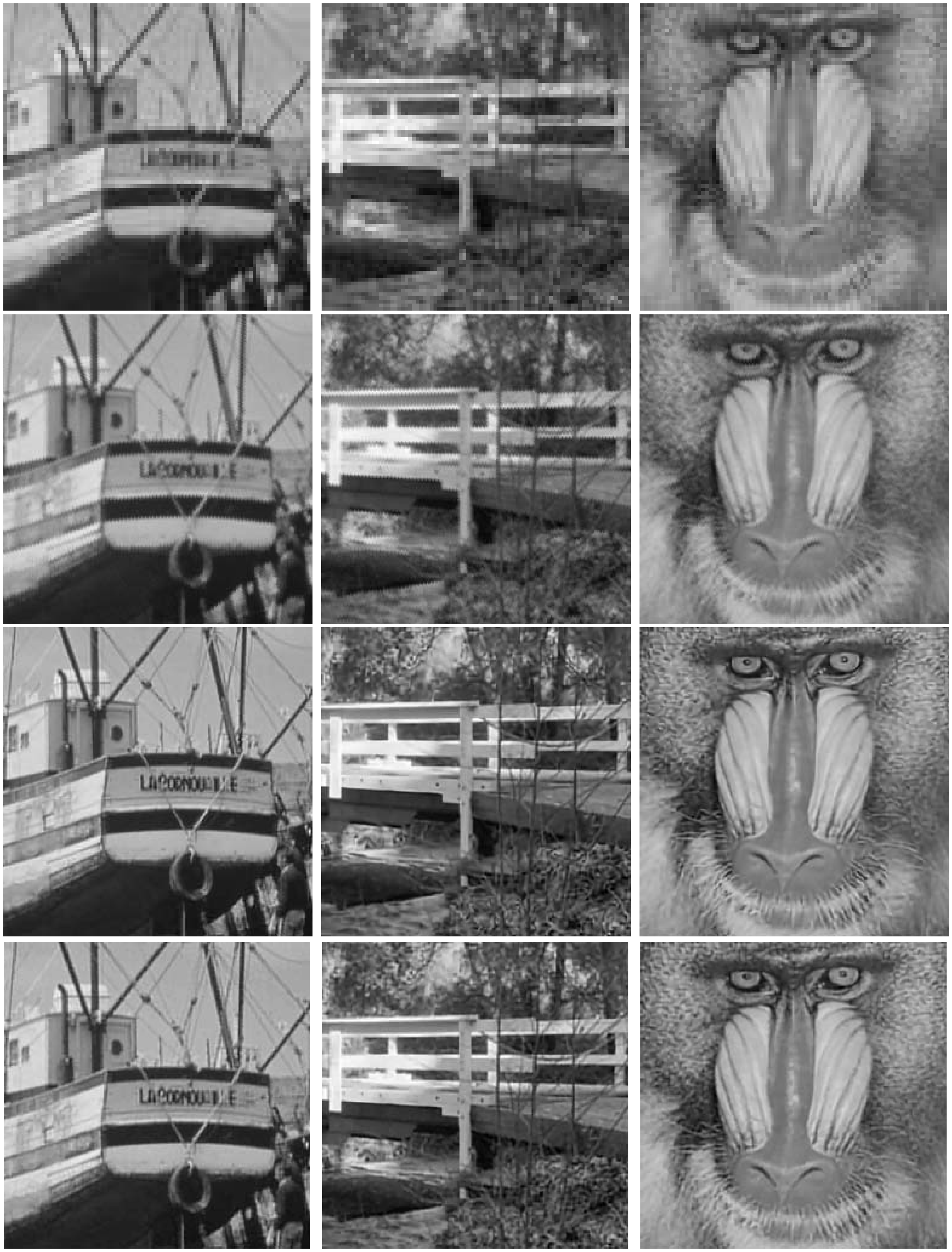

Figure 5: From top to bottom, the $(0, 0)$-th LR images, the observed HR images, and the reconstructed HR images for 3×3 sensor array. The reconstructed HR "Boat" image, "Bridge" image, and "Baboon" image by using Algorithm 1 (the third row) have PSNR = 31.87, 26.94 dB, and 27.59 dB respectively. The reconstructed HR "Boat" image, "Bridge" image, and "Baboon" image by using Algorithm 2 (the forth row) have PSNR = 31.38, 26.49 dB, and 27.17 dB respectively.

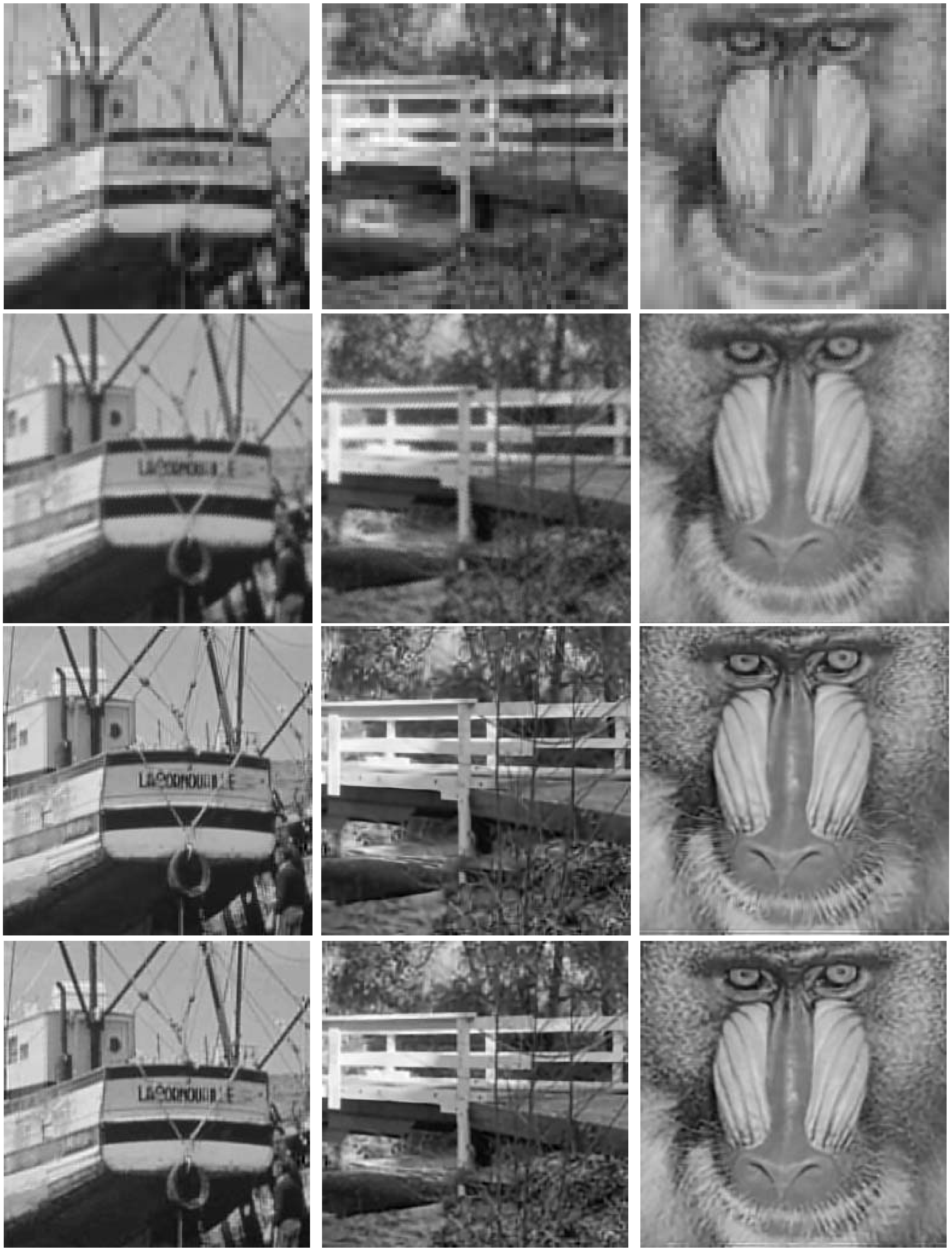

Figure 6: From top to bottom, the $(0, 0)$-th LR images, the observed HR images, and the reconstructed HR images for 4×4 sensor array. The reconstructed HR "Boat" image, "Bridge" image, and "Baboon" image by using Algorithm 1 (the third row) have PSNR = 30.83 dB, 25.85 dB, and 26.24 dB respectively. The reconstructed HR "Boat" image, "Bridge" image, and "Baboon" image by using Algorithm 2 (the forth row) have PSNR = 30.37, 25.48 dB, and 26.07 dB respectively.

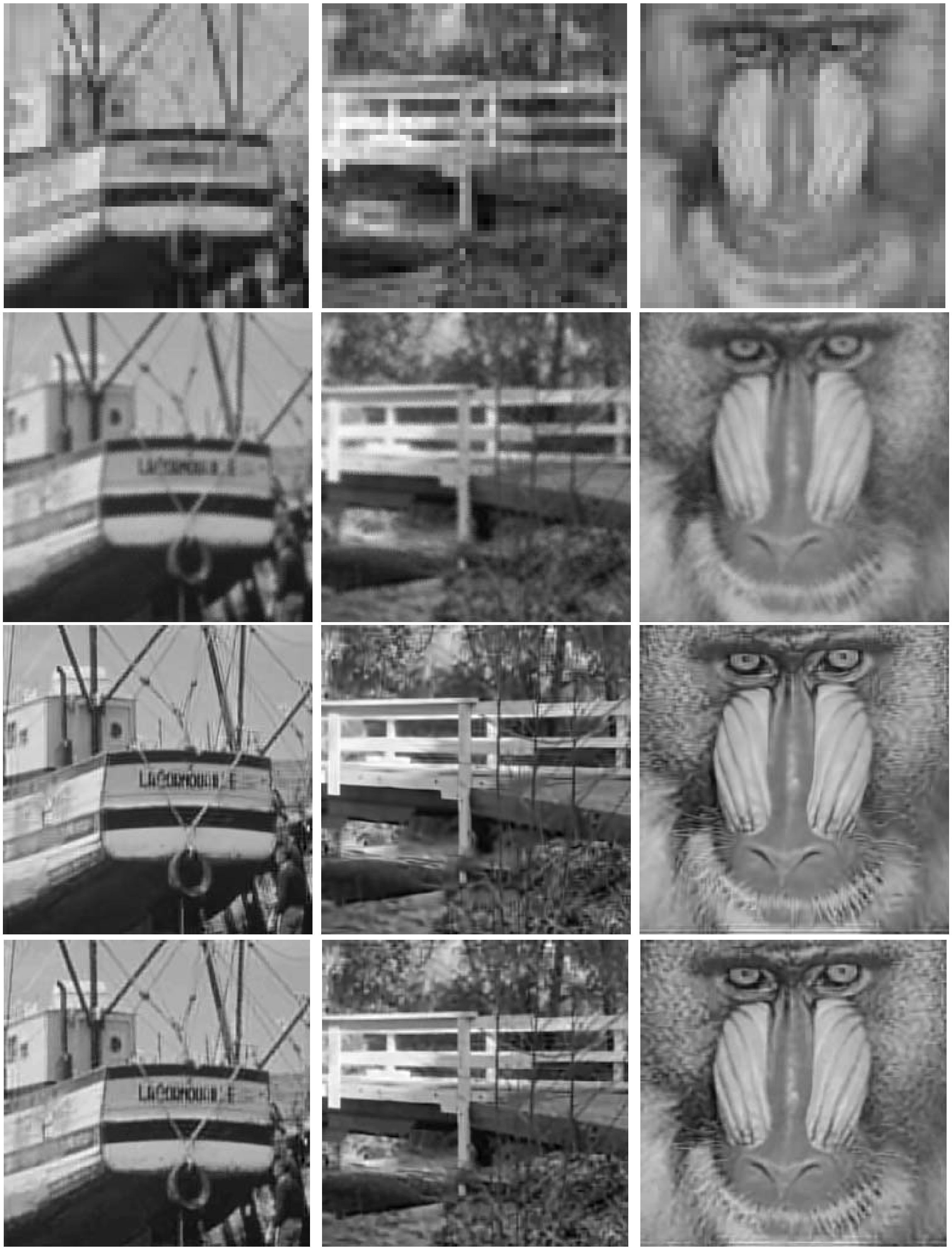

Figure 7: From top to bottom, the $(0,0)$-th LR images, the observed HR images, and the reconstructed HR images for 5×5 sensor array. The reconstructed HR “Boat” image, “Bridge” image, and “Baboon” image by using Algorithm 1 (the third row) have PSNR = 30.01 dB, 25.01 dB, and 25.81 dB respectively. The reconstructed HR “Boat” image, “Bridge” image, and “Baboon” image by using Algorithm 2 (the forth row) have PSNR = 29.42, 24.76 dB, and 25.49 dB respectively.